Mass removal and clay mineral dehydration/ rehydration in carbonate-rich surface exposures of the 2008 Wenchuan Earthquake fault: Geochemical evidence and implications for fault zone evolution and coseismic slip

Jianye Chen,[1,2] Xiaosong Yang,[1] Shengli Ma,[1] and Christopher J. Spiers[2]

[1] We report variations in the mineralogical, geochemical, and isotopic ($\delta^{13}C$, $\delta^{18}O$) composition of fault rocks sampled in transects across the Zhaojiagou and Pingxi exposures of the Wenchuan Earthquake or Longmenshan Fault Zone, where the gouge-rich fault core and principal slip surface cuts through carbonate-rich strata. Pervasive fluid infiltration was found to modify the mineralogical and geochemical architecture of the fault zones studied. Enrichment/depletion patterns, element partitioning, and a very large implied volume loss are quite different from those characterizing faults in granites and clastic sedimentary rocks and can be explained by a mass removal model involving dissolution and advective transport enhanced by pressure solution. An increasing enrichment in smectite observed toward the principal slip surface, a high abundance of elements such as Ba, Mg, and F, the deposition of minerals such as barite and fluorapatite, as well as the distinct depletion in ^{13}C in vein material consistently suggest reactions involving a hydrothermal fluid originating at depth. Illitization of black gouges, caused by coseismic frictional heating, was found to be widespread. We propose that coseismic frictional heating along with the action of postseismic hydrothermal fluids controlled the transformation and distribution of smectite and illite within the fault core of the Longmenshan Fault Zone. The coseismic dewatering reactions are expected to have been more extensive at depth, possibly helping generate excess pore pressure assisting dynamic slip weakening during the Wenchuan Earthquake.

Citation: Chen, J., X. Yang, S. Ma, and C. J. Spiers (2013), Mass removal and clay mineral dehydration/rehydration in carbonate-rich surface exposures of the 2008 Wenchuan Earthquake fault: Geochemical evidence and implications for fault zone evolution and coseismic slip, *J. Geophys. Res. Solid Earth*, *118*, 474–496, doi:10.1002/jgrb.50089.

1. Introduction

[2] The structure of the upper portion of brittle faults can generally be divided into three principal zones: the fault core, the surrounding damage zone, and the host rock (HR) [*Caine et al.*, 1996]. The fault core, where most of the displacement is accumulated, is characterized by comminuted rocks, such as fault gouge, which are typically subject to geochemical and mineralogical alteration during both coseismic and postseismic periods [*Kerrich et al.*, 1984; *Hickman et al.*, 1995]. Investigation of fault zone composition provides insight into fault strength, fluid flow, and fluid-rock interaction. Extensive studies have been performed on fault zones cutting crystalline and clastic sedimentary rocks [e.g., *Goddard and Evans*, 1995; *Tanaka et al.*, 2001; *Boullier et al.*, 2004]. However, relatively little work has been done on the geochemical signature of carbonate-hosted fault rocks. That which has been done [e.g., *Kirschner and Kennedy*, 2001; *Faulkner et al.*, 2003; *Labaume et al.*, 2004; *Janssen et al.*, 2005; *Molli et al.*, 2010; *Fondriest et al.*, 2012] suggests that the internal structure of carbonate fault zones is strongly influenced by chemical processes associated with fluid channeling and fluid-rock interaction.

[3] The permeability of fault zones can often be several orders of magnitude different from the HR [*Wibberley and Shimamoto*, 2003]. Fault zones accordingly exert an important control on subsurface fluid flow, acting as conduits for or as barriers to flow or even fulfilling a combined fault-valve function [*Sibson*, 1990]. Fluids in fault zones are thought to play a key role in earthquake nucleation and seismic rupture propagation [e.g., *Sibson*, 1973; *Chester et al.*, 1993; *Hickman et al.*, 1995]. For example, frictional heating and dehydration of water-bearing minerals can result

---

[1]State Key Laboratory of Earthquake Dynamics, Institute of Geology, China Earthquake Administration, Beijing, China.
[2]HPT Laboratory, Department of Earth Sciences, Utrecht University, The Netherlands.

Corresponding author: J. Chen, State Key Laboratory of Earthquake Dynamics, Institute of Geology, China Earthquake Administration, Beijing 100029, China. (jychen@ies.ac.cn)

in fluid pressurization that reduces the effective pressure acting on the fault plane, producing a mechanical weakening [*Brantut et al.*, 2008, 2011]. Fluids also play an important role in the chemical and architectural evolution of fault zones. Using bulk rock chemical analysis, *Goddard and Evans* [1995] concluded that fluids passing through fault zones react with the fault rock, dissolving and transporting soluble cations away. Such an effect can change fault rock volume, insoluble content and isotopic composition, as well as transport and mechanical properties [*Labaume et al.*, 2004; *Chen et al.*, 2007; *Molli et al.*, 2010; *Pili et al.*, 2002, 2011]. Similarly, fluid-assisted mineralogical changes may cause fault weakening and reactivation [e.g., *Chester et al.*, 1993], particularly when clay minerals are formed [e.g., *Wintsch et al.*, 1995; *Vrolijk and van der Pluijm*, 1999]. Fault gouges are often enriched in clay minerals with respect to the HR, as seen in the cores of seismogenic faults such as the Chelungpu Fault [*Isaacs et al.*, 2007] or the San Andreas Fault [*Lockner et al.*, 2011], where smectites are the most abundant clay minerals. Last, high-temperature fluids derived from coseismic heating may interact with fault rocks, changing isotopic ratios [*Kerrich et al.*, 1984; *Ishikawa et al.*, 2008]. These ratios are expected to record the *in situ* precipitation environment and to provide better indications of the origin of the fluid phase [*Wang et al.*, 2010] than elemental abundance.

[4] Alongside these observations on natural fault rocks, the manner in which mineral reactions interact with the faulting process has recently been observed experimentally. Alteration processes such as the smectite-illite transformation have been shown to result from coseismic frictional heating [*Hirono et al.*, 2008; *Kuo et al.*, 2009]. Coseismic mineral decomposition processes, such as dehydration of smectite or gypsum [*Ferri et al.*, 2010; *Brantut et al.*, 2011], dehydroxylation of kaolinite, and decarbonation of calcite or siderite [*Hirono et al.*, 2006; *Han et al.*, 2007; *Tanikawa et al.*, 2007], have also been demonstrated experimentally, corroborating natural evidence for such reactions seen, for example, in drill cores from the Chelungpu [*Mishima et al.*, 2006; *Hirono et al.*, 2008; *Hamada et al.*, 2009] and Nojima [*Famin et al.*, 2008] faults. Experiments are also showing that syndeformational mineral reactions and associated energy consumption may be much more important than previously recognized [*Brantut et al.*, 2011] as well as showing how reactions induced by frictional heating liberate fluid into the pores, building up pore pressure that may lead to dynamic stress reduction [e.g., *Ferri et al.*, 2010].

[5] Against this background, examining the mineralogical and chemical composition of fault rocks can be expected to yield key insights into the characteristics of the fluid associated with faulting as well as into the rock-fluid interaction processes that influenced the faulting mechanism. In this article, we report mineralogical (bulk composition and clay portion) and geochemical (major and trace elements) variations measured in transects across two surface exposures of the 2008 Wenchuan Earthquake rupture within the Longmenshan Fault Zone (LFZ), where the main slip surface cuts through carbonate-rich rocks. We document major mass/volume loss and element mobility in the fault rocks studied. A model describing the volume changes resulting from fluid-rock interaction in carbonate-rich fault zones is proposed.

We also determine the stable isotope ($\delta^{13}C$ and $\delta^{18}O$) ratios characterizing the fault rocks from one site by investigating the fault-related carbonate minerals. We go on to test models for isotopic evolution based on a decarbonation versus a water-rock interaction mechanism. In addition, the origin of the clay minerals within the fault zone and their role in the faulting process are discussed. It is argued that black gouge found at the sites studied was formed by illitization of smectite due to frictional heating and that the fluid released may have assisted dynamic rupture at shallow levels during the Wenchuan Earthquake.

2. Study Area and Methods

2.1. Study Area and Key Exposures

[6] The Longmenshan fault system constitutes of three parallel subfaults. From west to east, they are the Maoxian-Wenchuan, Yinxiu-Beichuan, and Guanxian-Jiangyou faults (Figure 1). The catastrophic Wenchuan Earthquake (M_s 8.0) of 12 May 2008 occurred on the Yinxiu-Beichuan Fault, producing a 240-km-long surface rupture [*Xu et al.*, 2009]. In this study, two exposures on the north segment of this fault are systematically investigated, the Zhaojiagou (ZJG) and Pingxi (PX) exposures. Both the principal coseismic slip surface at the ZJG and PX exposures cut through carbonate or carbonate-rich layers. Previous studies of microstructure, permeability, grain size distribution, frictional properties, and magnetic properties of the fault rocks at the two localities [*Fu et al.*, 2008; *Han et al.*, 2010; *Chen et al.*, 2011; *Yao et al.*, 2011; *Yang et al.*, 2012] show similar characteristics that may represent common features along much of the LFZ, at least along the north segment where similar internal structure and lithologies are involved in the fault.
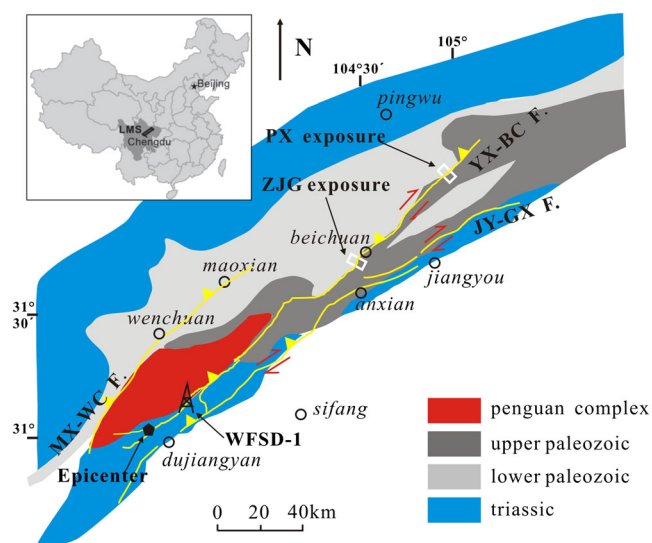
Figure 1. Location of the studying area and regional geological map of the Longmenshan (LMS) fault system consisting of three fault zones: the Jiangyou-Guanxian fault (JY-GX F.), Yingxiu-Beichuan fault (YX-BC F.), and Maoxian-Wenchuan fault (MX-WC F.).

2.2. Field Methodology

[7] To determine the internal structure and composition of the fault zone, transect sampling was employed at the two exposures. A roughly 50-cm-thick surface layer was removed to eliminate weathered rock. Samples were then collected at a spacing of <0.5 m across the exposed fault zone. Typical country rocks were also collected. Sampling density was reduced to ~1 cm near the principal slip surface. Oriented gouge samples from the main slip zone (MSZ) were collected for petrographic analysis. They were recognized as very fine grained, tacky, clay-rich material exhibiting ductile behavior when wet. This material was easily distinguishable from the surrounding rocks by its appearance, feel, and color. The surrounding damage zone, characterized by an increased density of crushed or fragmented grains and fractures relative to the HRs, was divided into a highly damaged zone (HDZ) and a weakly damaged zone (WDZ). The fault core, with a width of several decimeters [*Billi*, 2005], was recognized and defined as the combined HDZ and the fault gouges. The WDZ is defined by the portion of transect extending from the outside edge of the fault core (HDZ and the fault gouges) to the point at which the rock is marked by the appearance of bedding. This correlated with a notable decrease in fracture density and degree of alteration as well as changes in the dominant deformation pattern.

2.3. Laboratory Analyses

[8] Only fresh samples were selected for mineralogical and geochemical analysis. X-ray diffraction (XRD) was used to determine relative mineral content, including semiquantitative analysis for clay minerals. Unoriented, hand-powdered bulk samples were scanned over a 2θ range of 3–45° with CuKα radiation (0.15418 nm), at a scan rate of 2°/min with step width of 0.02°, employing a Dmax 12 kW X-ray power diffractometer (45 kV and 100 mA). Bulk powder samples gave a first evaluation of the relative amounts of bulk clays, whose proportion was further verified by analyzing the clay-sized portion (<2 μm). This was separated by centrifugation. Slurry samples (1 ml) of clays and distilled water were air-dried on glass slides and scanned over a 2θ range of 2.5–15°. Ethylene glycol was used to detect the swelling components with 2θ coverage of 2.5–30°. Heating the samples to 550°C also helped distinguish kaolinite from chlorite. For this, a 2θ coverage of 2.5–15° was used. The method of semiquantitative analysis of clay minerals followed *Syunnan* [1981] and *Lin et al.* [1992].

[9] For comparative purposes, identical samples to those used for XRD analysis were also used for geochemical analysis. Crushed sample material (~50 g) was powdered in an agate ball mill to <200 mesh grain size and then analyzed by X-ray fluorescence (XRD) spectrometry for major and minor oxides, including SiO_2, Al_2O_3, $Fe_2O_3^T$, K_2O, MnO, MgO, CaO, Na_2O, TiO_2, and P_2O_5, using a Magix-pro2440 XRF machine. The FeO content of the samples was determined by titration using $K_2Cr_2O_7$ after being digested by H_2SO_4 + HF [*Rao and Govil*, 1995]. Volatile components were measured by thermogravimetric analysis [*Tanaka et al.*, 2001]: primarily, water (presented as "H_2O") was determined by baking the samples at 110°C and recording the weight increase of 100% sulfuric acid in a chamber connected to the baking vessel. Weight loss after ignition at 1000°C for 3 h was also measured and presented as loss on ignition (LOI) data. Content of CO_2 was measured by nonaqueous titration [*Johnson et al.*, 1985]. The weight ratio of major elements, minor elements, H_2O, and LOI were combined and normalized to 100 wt.%. As for trace elements, the samples were first digested using distilled HF + HNO_3 in Teflon vessels and the percentages of trace elements were then determined using inductively coupled plasma-mass spectrometry (ICP-MS) employing a Thermoelemental X7 analyzer. Sample-digesting procedures, analytical precision, and accuracy of ICP-MS analyses are the same as described by *Li et al.* [2006]. All geochemical tests were conducted at Hubei Geological Research Laboratory.

[10] To quantify the element transfer and volume loss/gain within the LFZ, correlation analysis and the isocon method were applied [*Grant*, 1986; *Tanaka et al.*, 2001]. The isocon approach involves plotting element concentration in an altered sample (or mean of a group of altered samples) against an unaltered reference precursor, in a "Grant-type plot" [*Grant*, 1986]. Elements that are immobile should be dispersed along a straight line passing through zero. These elements are usually high-field strength elements, because they are expected to be less mobile or fully immobile in fluid-rock interaction and weathering processes [*Goddard and Evans*, 1995]. In our study, TiO_2 as the most used reference elements [e.g., *Tanaka et al.*, 2001; *Chen et al.*, 2007] was chosen as the immobile proxy defining the isocon line, along which elements that are neither gained nor lost during alteration will fall. The slope of this line defines the net mass change of the altered sample. To quantify corresponding volume changes, grain densities were measured by pycnometry. Average densities of the HRs of material from the HDZ and from the MSZ are listed in Table 1.

[11] For the ZJG exposure, carbon and oxygen isotope analyses on fault-related calcite (breccia fragments, matrix and vein material) were performed. Powdered samples were obtained by microdrilling the hand specimens. Breccia fragments refer to fragments with diameter bigger than 1.5 mm so that drilling can be performed on individual particles. Matrix represents portion of the specimen in which the fragments is <0.5 mm. After dissolving in 100% H_3PO_4, the CO_2 gas released was collected for mass spectrograph analysis, employing the MAT 253 isotope-ratio mass spectrograph machine at the Institute of Geology, Chinese Academy of Geological Sciences. The isotopic compositions measured are reported in the δ-notation permil (‰) with a precision of ±0.2‰ using the V-PDB standard for $\delta^{13}C$ and the V-SMOW standard for $\delta^{18}O$, respectively.

3. Characterization of the Longmenshan Fault Rocks: Results of the ZJG Transect

3.1. Character of the Exposure

[12] The ZJG exposure is located 3 km southwest of Beichuan City (Figure 1). The fault zone exposure at this site was ~8 m wide and the coseismic slip offset was ~6.5 m thrust motion [*Xu et al.*, 2009]. The fault here strikes at an azimuth of 45° and dips 64–78° to the NW (Figure 2). The hanging wall protoliths consist of fine sandstones and carbonates, whereas the footwall is sandstone. The principal

Table 1. Average Bulk and Trace Element Composition Along With Grain Densities of the HR and the Rocks From the HDZ and the MSZ of the ZJG and PX Exposures[a]

Exposure	ZJG						PX					
	HR(5)	RSD	HDZ(4)	RSD	MSZ(2)	RSD	HR(4)	RSD	HDZ(4)	RSD	MSZ(4)	RSD
Na_2O	0.03	0.28	0.14	0.34	0.14	0.01	0.06	0.23	0.04	0.26	0.05	0.17
MgO	0.56	0.16	5.18	0.82	3.65	0.29	17.58	0.09	4.20	0.31	3.16	0.18
Al_2O_3	0.78	0.17	7.25	0.22	16.24	0.09	0.80	0.29	6.02	0.16	11.03	0.23
SiO_2	1.90	0.23	24.36	0.20	53.80	0.08	11.83	0.31	44.92	0.07	62.01	0.02
P_2O_5	0.03	0.00	0.10	0.37	0.16	0.14	0.14	0.42	0.30	0.23	0.47	0.42
K_2O	0.21	0.24	1.86	0.25	3.37	0.05	0.18	1.13	1.64	0.18	2.96	0.37
CaO	53.44	0.01	28.73	0.25	5.56	0.44	27.47	0.16	18.55	0.21	2.98	0.45
TiO_2	0.04	0.32	0.32	0.22	0.62	0.05	0.05	0.21	0.30	0.14	0.54	0.20
MnO	0.01	0.00	0.05	0.29	0.04	0.00	0.20	0.37	0.87	0.23	1.64	1.05
Fe_2O_3	0.13	0.10	1.80	0.32	3.75	0.12	0.44	1.19	2.62	0.11	5.41	0.14
$Fe_2O_3^T$	0.24	0.24	2.72	0.24	6.03	0.08	0.52	1.00	2.64	0.11	5.46	0.15
H_2O	0.41	0.10	2.09	0.20	4.15	0.04	0.60	0.38	1.96	0.16	3.66	0.06
CO_2	42.15	0.00	26.94	0.14	6.12	0.46	40.08	0.12	17.61	0.12	2.88	0.51
LOI	42.63	0.01	29.25	0.11	10.27	0.29	40.97	0.11	20.34	0.09	7.78	0.16
Trace[T]	0.07	0.10	0.16	0.26	0.26	0.07	0.19	0.37	0.87	0.24	2.27	0.51
Be	0.07	0.36	1.25	0.27	2.61	0.10	0.30	0.46	1.69	0.08	3.16	0.20
Sc	1.10	0.62	7.07	0.23	13.65	0.01	2.95	0.48	5.72	0.10	10.82	0.10
Cr	0.74	0.36	31.69	0.27	72.37	0.08	88.58	0.48	45.78	0.37	120.1	0.37
Co	1.42	0.06	7.85	0.25	14.58	0.03	3.22	0.43	16.20	0.43	47.38	0.56
Ni	16.13	0.07	22.68	0.14	39.99	0.10	46.34	0.52	198.2	0.54	261.7	0.88
Cu	2.51	0.14	20.62	0.68	26.71	0.08	23.20	0.23	44.10	0.31	93.50	0.53
Zn	4.82	0.40	32.99	0.21	81.35	0.09	8.51	0.25	268.9	0.21	351.2	0.67
Rb	13.87	0.36	108.58	0.30	204.5	0.13	8.40	0.35	71.02	0.08	131.2	0.36
Pb	2.19	0.39	10.97	0.39	14.74	0.06	13.45	0.30	26.57	0.24	40.00	0.12
Th	1.23	0.42	8.68	0.24	16.04	0.02	2.11	0.32	7.99	0.09	13.72	0.25
U	0.45	0.18	1.94	0.33	3.19	0.05	12.78	0.29	26.92	0.27	16.66	0.24
Sr	256.73	0.26	148.45	0.42	61.61	0.18	258.7	0.09	225.0	0.24	129.6	0.60
V	6.03	0.13	44.82	0.24	103.0	0.09	315.9	0.33	271.2	0.26	543.2	0.67
Zr	15.55	0.31	75.92	0.17	138.9	0.10	31.79	0.35	65.55	0.17	117.80	0.03
Nb	1.42	0.12	6.73	0.35	12.87	0.05	1.56	0.26	6.16	0.10	11.41	0.13
Ba	188.10	0.10	334.7	0.25	836.7	0.18	699.5	1.12	6160	0.29	1.87E4	0.57
Hf	0.55	0.18	2.39	0.16	4.33	0.13	0.80	0.32	1.85	0.11	3.57	0.07
F	156.40	0.10	661.6	0.39	852.2	0.03	465.6	0.45	1172	0.02	1849	0.11
B	4.73	0.29	56.61	0.50	127.1	0.01	12.27	0.54	54.38	0.05	132.9	0.40
Sn	0.43	0.49	1.39	0.27	3.36	0.06	0.31	0.15	1.34	0.05	3.30	0.64
Density	2.73		2.67		2.60		2.72		2.67		2.62	

[a]Major element data are in wt.%, trace element data are in ppm, and density is in g/cm^3. The figures in brackets are the number of samples for averaging. RSD is relative % of standard deviation (normalized by average value).

slip surface cuts through the carbonate layers. Different types of fault rocks occur across fault zone. From west to east, they are (1) fractured limestone, (2) weakly cemented coarse breccias, (3) coarse breccias, (4) weakly foliated fine breccias, (5) gray and dark black gouge, (6) weakly foliated fine breccias, (7) coarse breccias, and (8) fractured sandstone.

[13] The internal structure of the fault zone is relatively simple. Only one principal slip zone can be found and no branches exist. The width of the fault core is extremely narrow (~20 cm), consisting of ~2-cm-thick gray gouge in the center and weakly foliated yellowish crushed breccias besides (Figure 2b and 2c). An even thinner black gouge layer (~3 mm) is developed adjacent to the gray gouge. The black gouge was harder and less tacky than the gray one. The nonclay fault rocks were progressively cemented toward the fault center. As shown in Figure 2b, 2–5 cm-thick vein material occurred at the margins of the gouge zone. Occasionally, the gouges were partially cemented to form ultracataclasite.

3.2. Mineralogical Results

[14] Mineralogical analyses were performed on 29 samples across the ZJG exposure. Data on major and trace mineral composition are presented versus logarithmic distance from the principal slip surface in Figure 3. The black gouge is defined as the zero position. XRD analysis identified quartz, dolomite, calcite, and feldspar as major minerals. The content of quartz was found to increase and that of carbonates and feldspar to decrease toward the principal slip surface, and feldspar fell below detection in the MSZ. Approaching the principal slip surface, the clay content of bulk samples also increases remarkably, with a peak value of 34% for the gray gouge.

[15] Clay minerals in the <2 μm fraction of samples from the ZJG exposure were identified as mainly illite, mixed layers of illite-smectite (I/S), and chlorite, with no detectable smectite (one exception with 2%). As shown in Figure 3, the reference abundance of illite decreased gradually toward the principal slip surface (from 100% to 3%), whereas that of I/S showed the opposite trend (from 33% to 83%). Chlorite content in the fault core was <10%, whereas the footwall was characterized by much higher chlorite content (~50%). The mixlayer ratio (S%, the percentage of smectite in I/S) also increased notably toward the principal slip surface (from 5% to 38%). Data on the total content of smectite (denoted by S* = smectite + smectite contained in I/S) and
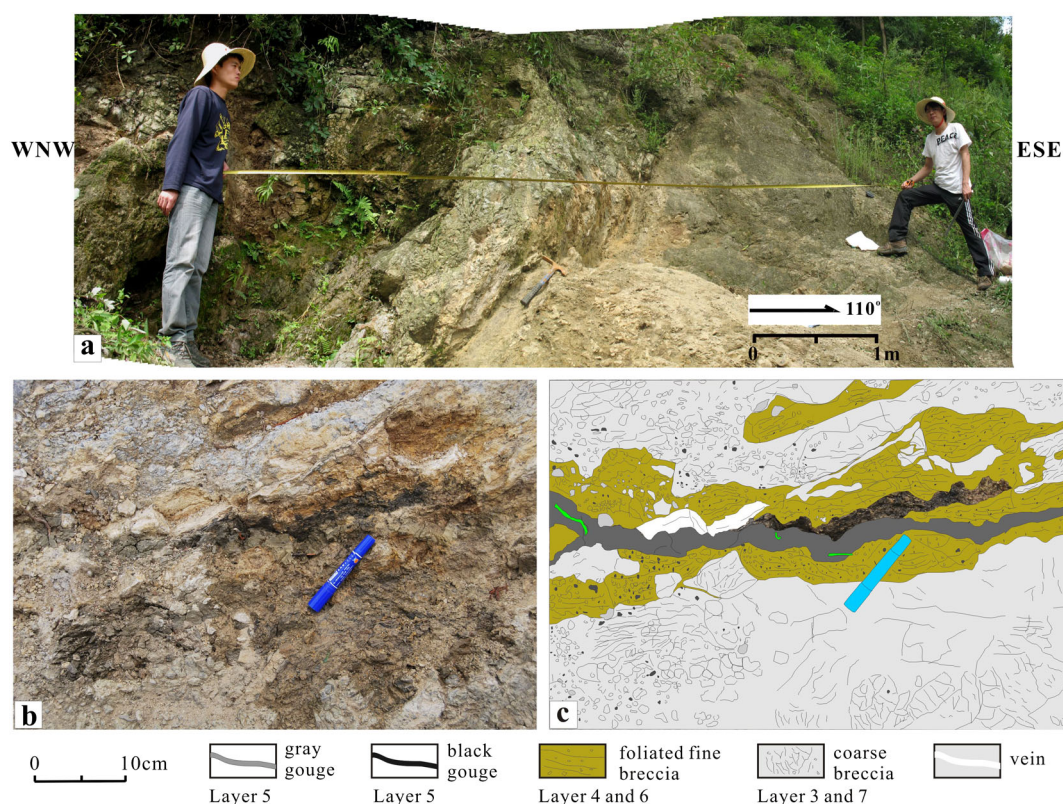
Figure 2. (a) Outcrop, (b) fault core structure, and (c) the interpretive sketch of the ZJG exposure on the LFZ (GPS location is 31°48′22.44″N, 104°25′57.61″E).

illite (denoted by I* = illite + illite contained in I/S) are also presented in Figure 3, indicating increasing enrichment of total smectite and depletion of illite within the fault core. It is worth noting that the gray and black gouges showed similar mineralogical compositions, except for their clay mineral content. The gray gouge contained slightly less quartz and more clay (Figure 3). The black gouge was characterized by higher illite content and less I/S with respect to the gray gouge.

3.3. Geochemical Results

[16] Bulk sample chemical compositions exhibited continuous variation across the exposure, especially in the fault core (Figure 4). The content of SiO_2, Al_2O_3, K_2O, TiO_2, $Fe_2O_3^T$, H_2O, and $Trace^T$ (weight percentage of all trace elements) were found to be increasingly enriched toward the principal slip surface, with the highest values for the gray gouge, whereas CaO, MgO, CO_2, and LOI behaved opposite. Nearly all trace elements showed enrichment in the fault core compared with the surrounding HRs (Figure 5). Within the fault core, all trace elements exhibited progressive enrichment toward the principal slip surface, with Sr as the only exception. This trend was consistent with that displayed by major elements such as Al_2O_3 and TiO_2 (Figure 4), and also by the bulk clay content (Figure 3). Among the trace elements, Ba and F showed relatively high abundance, with maximum values of 920 and 1050 ppm, respectively. The gray gouge and black gouge had almost the same trace element compositions. However, for major elements, the black gouge showed slightly lower content of Al_2O_3, K_2O, and TiO_2 and higher content of MgO.

[17] At the ZJG exposure, nearly all elements showed positive correlation coefficients with the content of TiO_2, except for CaO (r = −0.94), MgO (r = −0.36), and CO_2 (r = −0.97) among the major elements and Sr (r = −0.66) among the trace elements. The samples selected for isocon analysis are denoted in the subplot of TiO_2 of Figure 4 and the average elemental abundances of the HR, the HDZ, and the MSZ are listed in Table 1. Grant-type plots (Figure 6) showed the following results:

[18] 1. The fault rocks within the HDZ (Figure 6a) and MSZ (Figure 6b) showed obvious enrichment in nearly all elements analyzed compared with the HR, except for CaO, CO_2, and Sr. Data points for SiO_2, MgO, Al_2O_3, K_2O, $Fe_2O_3^T$, and even H_2O for major elements and Co, Th, Be, Zr, Zn, V, Nb, Pb, Se, Cu, K, Rb, and U for trace elements, as covered by the shading in Figures 6a and 6b, fall fairly close to the isocon line of TiO_2, exhibiting a consistent enrichment signature and also suggesting a high confidence level of our analysis.

[19] 2. A few elements (i.e., Ba, Ni, Na_2O, P_2O_5, F, and Cr) deviate from the isocon line.

[20] 3. As shown in Figures 6a and 6b, the HDZ is 8.3 times enriched in content of TiO_2 and the estimated volume loss was 87% relative to the HR. The MSZ is 15.8 times enriched and the volume loss was 93%.

[21] 4. The inclination of the isocon line for the MSZ was 1.9 times greater than that for the HDZ (Figure 6c), indicating increasing volume loss toward the principal slip center.
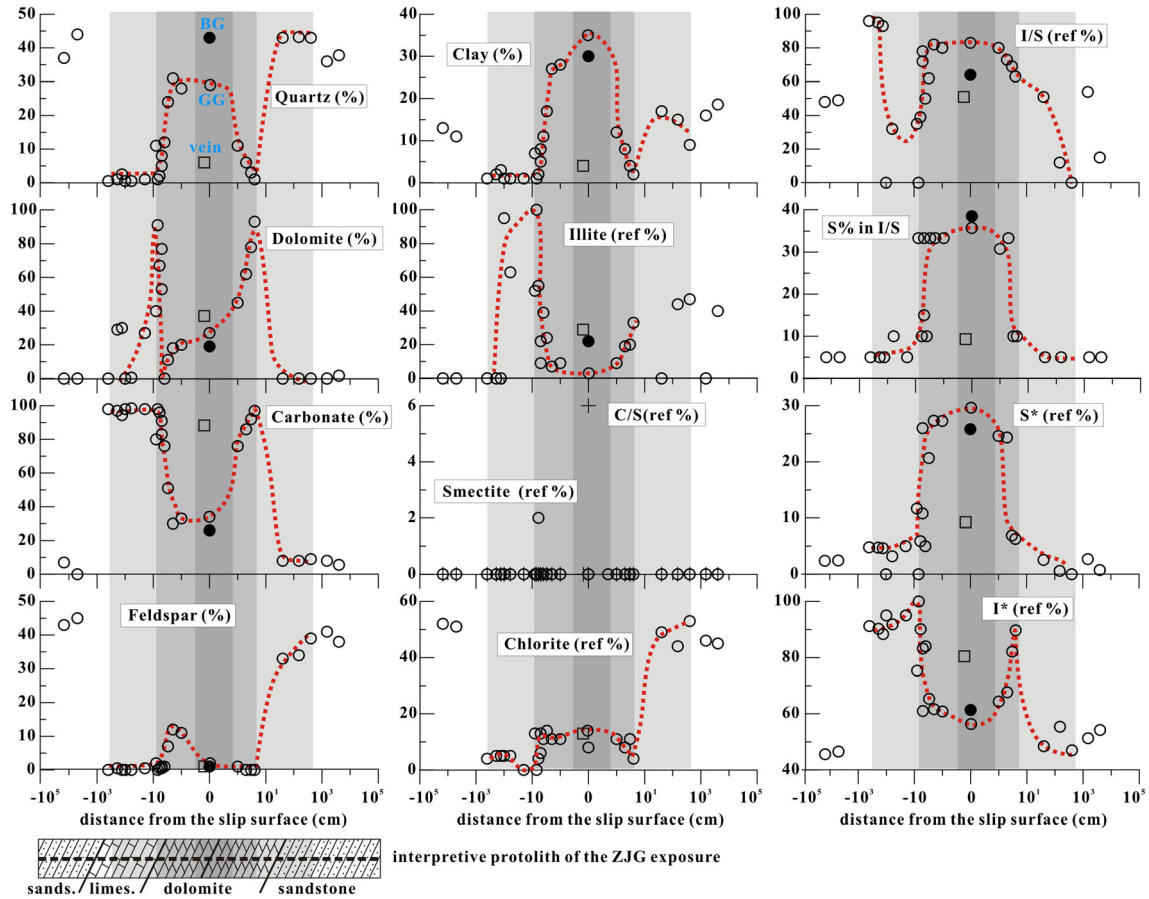
Figure 3. Variation in bulk and clay mineral (<2 μm) composition across the ZJG exposure of the LFZ. Different shaded domains, from light to dark, indicate the WDZ, the HDZ, and the MSZ, respectively. The dashed lines are the interpretive varying trends. Two data points are exhibited at x = 0, representing the gray gouge (GG) and black gouge (BG). The latter is denoted by solid circles. The squared symbols represent the veins besides the gouge samples. The content of an individual clay mineral is presented in reference content (ref%) accounting for the total clay. S* is the total content of smectite (S* =smectite + smectite contained in I/S), whereas I* is the total content of illite (I* = illite + illite contained in I/S).

3.4. Isotopic Characteristics

[22] Stable isotopic compositions (δ^{13}C and δ^{18}O) of breccia fragments, matrix and vein material from the fault core, as well as the country rocks (protoliths) were investigated. As shown in Figure 7, the isotopic compositions of the breccia fragments are distinct from that of the matrix and vein material by a δ^{13}C value of −4‰. Overall, the δ^{13}C values decreased progressively for breccia fragments, matrix, and vein material collected from the same specimen (an example of this trend is denoted by the solid line in Figure 7). The lowest δ^{13}C and δ^{18}O signature of the fault rocks was shown by vein material (δ^{13}C = −8.0‰ and δ^{18}O = 19‰) located directly adjacent to the fault gouge (Figure 2). The values of δ^{18}O of the breccia fragments (19.7–27.8‰) are generally greater than that of the matrix and vein material (19–21‰). The δ^{13}C and δ^{18}O values for the breccia fragments displayed a range that is consistent with those plotted in Figure 7 for the protolith in the hanging wall (limestone). The sandstone data (protolith of the footwall) plot far away from both the limestone and fault rock data.

4. Characterization of the Longmenshan Fault Rocks: Results of the PX Transect

4.1. Character of the Exposure

[23] The PX exposure is located near the northeast terminus of the surface rupture trace (Figure 1). The exposure at this site was ~9 m wide (Figure 8a). The fault plane exhibited slightly reversed inclination, dipping ~71° toward the footwall instead of toward the hanging wall. The coseismic thrust and right-lateral shear displacements were ~2.0 and 3.0 m, respectively [Li et al., 2010]. The rocks surrounding the fault core are fine sandstone. However, field and hand specimen analysis coupled with petrography indicated that the principal slip of the Wenchuan Earthquake must have cut through the carbonate-rich layers. This was further confirmed by the finding that the fault core is enriched in carbonate minerals. Recognizable fragments of limestone are present in the fault breccias in the damaged zone, mixed with sandstone fragments. Tracking along-strike indicated spatial continuity of the internal structure and lithology of the fault zone. From west to east, different types of fault
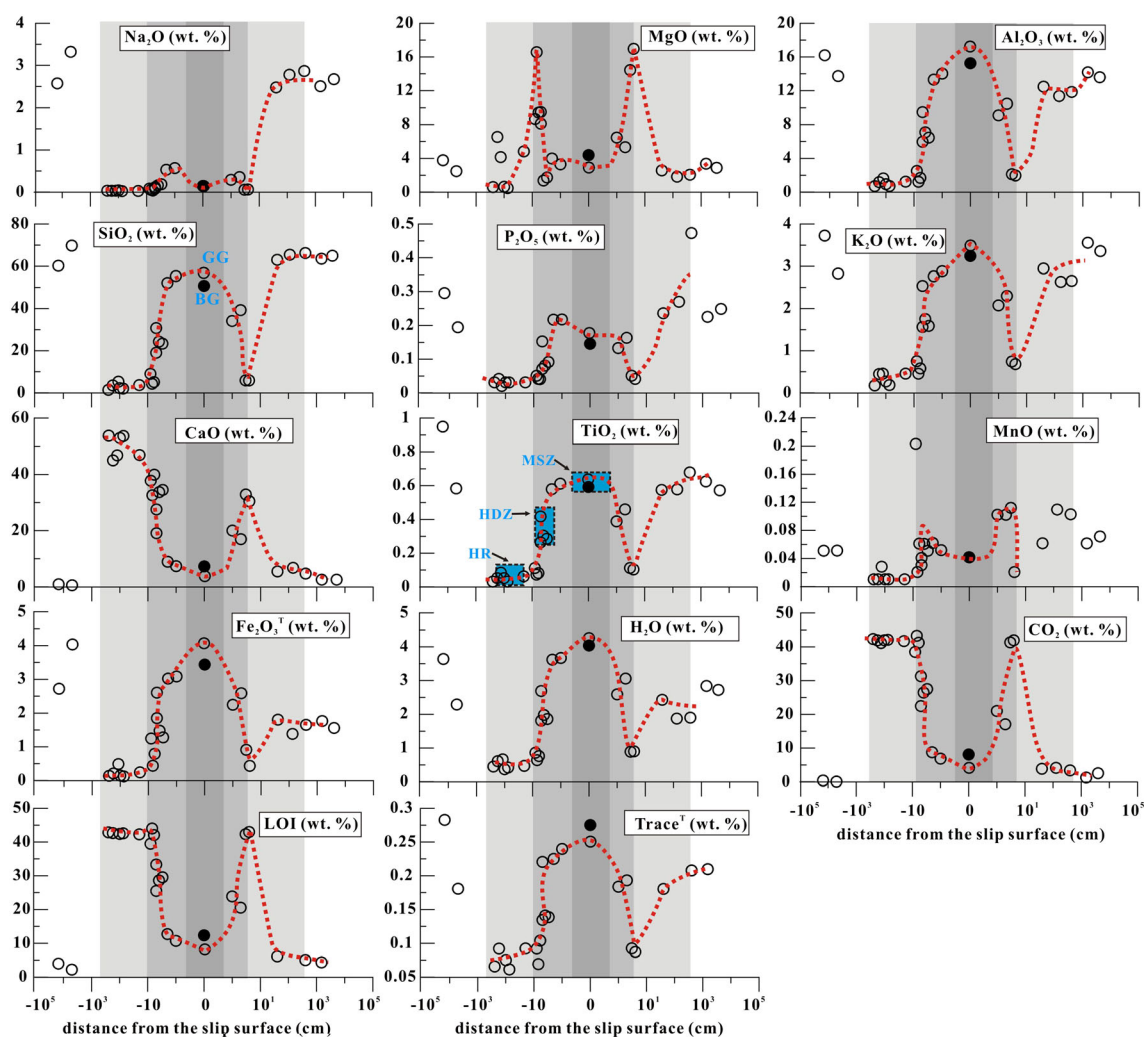
Figure 4. Concentration profiles of the bulk elements across the ZJG exposure. The blue dashed squares in the subplot of TiO₂ denote the selected samples for isocon analysis (in Figure 6), representing the HR, the HDZ, and the MSZ, respectively. Trace[T] = total concentration of trace elements. Other detailed content as in Figure 3.

rocks occurred within the fault zone: (1) coarse breccias (>2.5 m), (2) brownish gouge (15–25 cm), (3) gray or dark black gouge (0.5–3.5 cm), (4) yellowish gouge (~15 cm), (5) black breccias (~30 cm), (6) coarse breccias (1.5–2.5 m), and (7) fractured sandstone (>4.0 m).

[24] The width of the fault core (Layers 2–4) is ~40 cm. As shown in Figure 8b and 8c, the principal slip of the Wenchuan Earthquake occurred in Layer 3, which contrasted highly with the surrounding rocks. This was confirmed by continuous slicing analysis. Layer 3 occasionally cut through the brownish gouge (Layer 2) and yellowish gouge (Layer 4), which may record deformation inherited from past fault motion, presumably reflecting repeated earthquakes [*Caine et al.*, 1996]. It is interesting that the color of the principal slip gouge varied with thickness. It exhibited a gray color when thick (~2.5 cm) and turned black when thinner than 7 mm. As at the ZJG exposure, the gray gouge was wetter, softer, and much tackier than the black gouge.

[25] Fragments of vein material were found widespread along the fault core boundaries (Figure 8c). On the hanging

wall, a manganese-rich layer occurs ~3 m away from the slip surface (local people have exploited this as manganese ore for many years). This was totally black and 15–20 cm wide in this exposure. However, its width varies laterally. Its occurrence follows the fault rupture trace for at least ~3 km. Mineralogical and geochemical data showed that it is composed of kutnohorite, fluorapatite, and quartz and that the average content of MnO is ~21 wt.%.

4.2. Mineralogical Results

[26] At the PX exposure, 40 samples were collected for mineralogical analysis. XRD analysis identified quartz, dolomite, and calcite as major minerals and K-feldspar, fluorapatite, goethite, and gypsum as trace minerals (Figure 9). Samples from the fault core contain more carbonate minerals than other portion of the fault zone, demonstrating a carbonate protolith for the fault core. Within the fault core, the content of carbonates decreases, whereas quartz content increases approaching the principal slip surface. Barite was abnormally concentrated in the fault zone with a maximum value of 6.0%. The profile showed one barite peak at the fault core
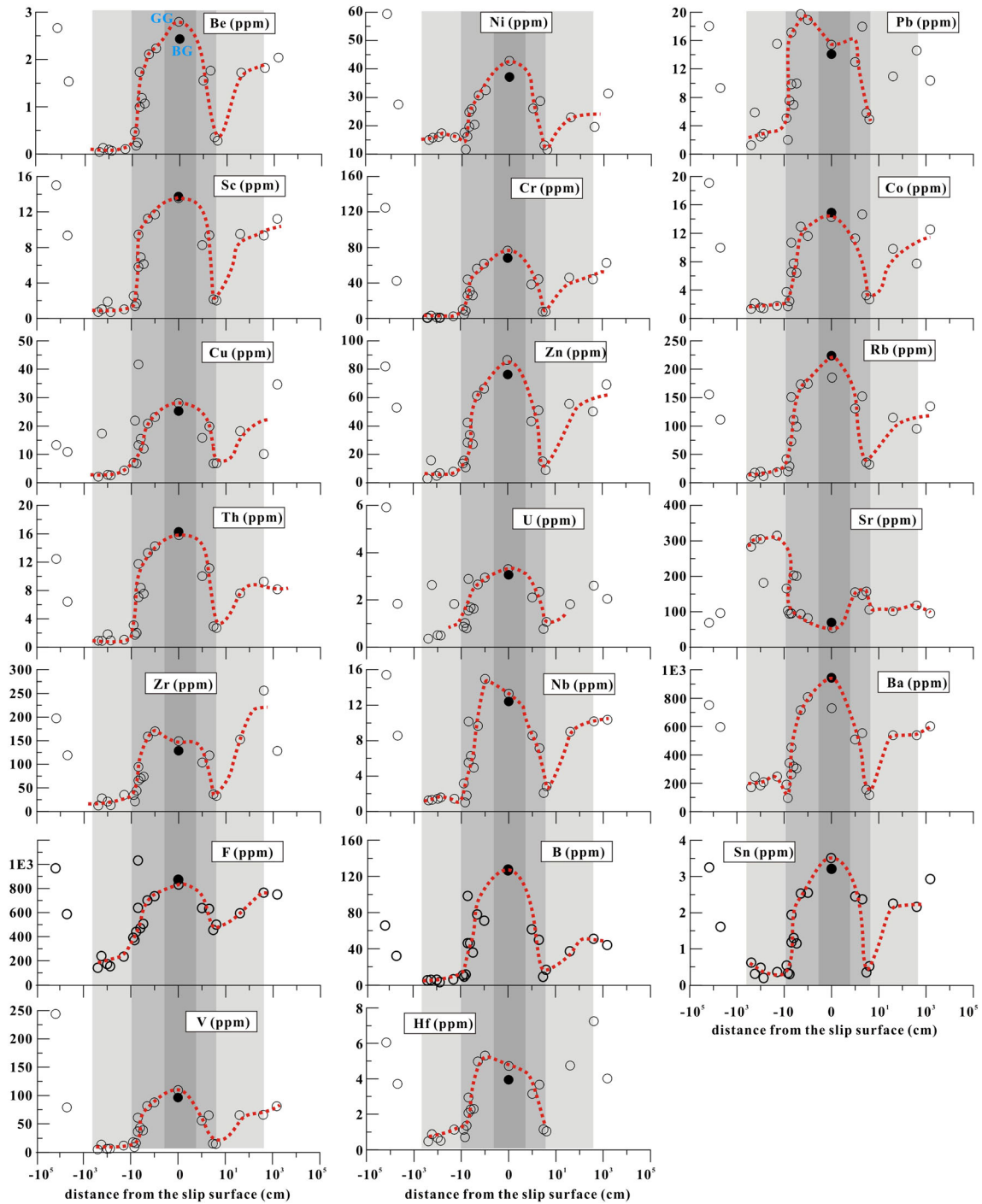
Figure 5. Concentration profiles of the trace elements across the ZJG exposure. Other detailed content as in Figure 3.

boundary and another in the MSZ. Other trace minerals such as gypsum and fluorapatite were also enriched at the fault core boundary.

[27] The clay content of bulk samples increased notably toward the principal slip surface (Figure 9), with a peak value of 25% for the gray gouge. Detailed semiquantitative analysis showed that the clay minerals at the PX exposure were mainly smectite and illite with minor halloysite (Halloysite is often found near carbonate rocks and it is usually taken as a typical product of hydrothermal alteration

[Kerr, 1952].) As shown in Figure 9, the profile for smectite resembled that of barite. Despite a sharp peak at the hanging wall, smectite showed clear enrichment toward the principal slip surface, whereas illite exhibited the opposite trend. Halloysite occurred near the margins of the fault core and disappeared below detection in the MSZ. As at the ZJG exposure, the gray gouge and black gouge showed rather different clay composition, although their bulk mineral compositions were similar to each other. The gray gouge contained slightly less quartz and more clay with respect to
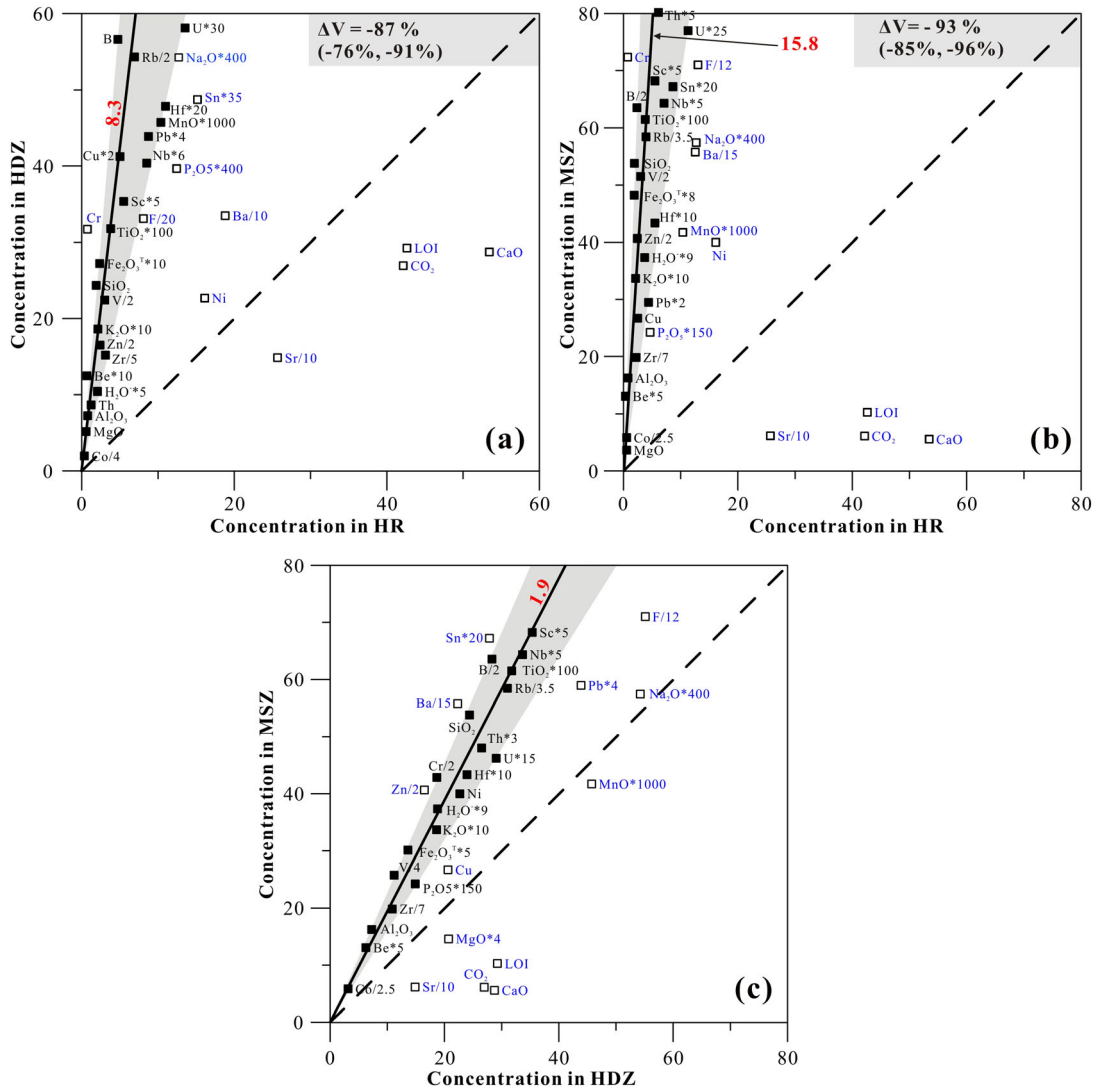
Figure 6. Grant-type plots for the HR against the HDZ and the MSZ as well as the HDZ against the MSZ at the ZJG exposure. Concentrations are noted for major elements in wt.% and for trace elements in ppm and scaled to the plot. The solid lines are the isocon lines for TiO_2, and the solid symbols (within the shaded area) represent the elements whose compositions are close to the isocon line. The dashed lines are the equilibrium lines, indicating neither enrichment nor depletion. See Table 1 for more details of the chemical composition. ΔV (%) indicates the percentage volume loss relative to the HR. The two values in brackets are the volume loss corresponding to the lower and upper bounds of the shaded area.

the black gouge. The reference abundances of smectite were 32.0% for the gray gouge, whereas the black gouge was characterized by the disappearance of smectite. The data of smectite content for the gray gouge seems to match well the trend seen across the entire PX exposure, whereas the black gouge was far away from that trend.

4.3. Geochemical Results

[28] Thirty-eight samples from the PX exposure were selected for geochemical analysis. As shown in Figure 10, the variation profiles of SiO_2, CaO, MgO, and CO_2 across the fault zone well match the interpreted carbonate protolith (Figure 9), with higher content of CaO, MgO, and less SiO_2 in the fault core. This interpretation is consistent with hand-specimen study and petrography as well as the mineralogical results. As for the variation profile obtained for barite content

(Figure 9), those for MnO, $Fe_2O_3^T$, and P_2O_5 showed two peaks. With the exception of CaO, MgO, CO_2, and MnO, the profiles for Al_2O_3, K_2O, TiO_2, P_2O_5, $Fe_2O_3^T$, H_2O, and, to a lesser extent, Na_2O and SiO_2 showed gradual enrichment toward the principal slip surface. Moreover, within the fault core, trace elements such as Be, Sc, Rb, Th, Zr, Nb, Hf, F, and B exhibited increasing enrichment toward the principal slip surface. In contrast, some elements (Cr, V, U, Sn, and Sr) showed gradual depletion toward the principal slip surface (Figure 11). The gouge samples displayed anomalous values deviating from the general trends of the fault core, being enriched in Cr, V, U, and Sr but depleted in Be, B, Sc, Rb, and Th (Figure 11). Among the trace elements, Ba and F showed anomalously high abundance (with maximum values of 5.4×10^4 and 2.1×10^3 ppm) in accordance with the profiles obtained for barite and fluorapatite content.
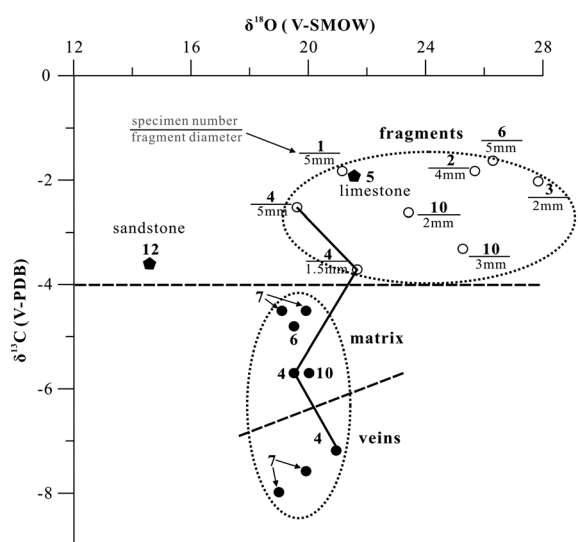
Figure 7. Stable isotope compositions ($\delta^{13}C$ and $\delta^{18}O$) of HRs, breccia fragments, matrix, and vein material at the ZJG exposure. The five-cornered stars represent different types of HRs. The open circles stand for breccia fragments, whereas solid circles stand for matrix and vein material. Overall, the $\delta^{13}C$ values decreased progressively for breccia fragments, matrix, and vein material collected from the same specimen, as denoted by an example in solid line.

[29] At the PX exposure, the concentration of TiO_2 showed positive correlation coefficients with that for Al_2O_3 (r = 1.00), K_2O (r = 0.90), and P_2O_5 (r = 0.42) among the major elements and for trace elements B (r = 0.86), Be (r = 0.89), F (r = 0.78), Sc (r = 0.97), Rb (r = 0.87), Th (r = 0.95), Zr (r = 0.85), Nb (r = 0.91), and Hf (r = 0.94). Negative correlations were obtained for MgO (r = −0.28), MnO (r = −0.14), CaO (r = −0.4), CO_2 (r = −4.3), and Sr (r = −0.02). The samples selected for isocon analysis are denoted in the subplot for TiO_2 in Figure 10. Grant-type plots (Figure 12) showed the following features:

[30] 1. As for the ZJG exposure, most elements showed enrichment and the data points fall fairly close to the isocon line, except for major elements MgO, CaO, CO_2, and trace element Sr (Figure 12a and b).

[31] 2. The data points for Zn and Ba fall well above the isocon line.

[32] 3. The HDZ was 6.0 times enriched and the calculated corresponding volume loss was 83% with respect to the HR (shaded area in Figure 12a). The MSZ showed 5.1–10.7 times enrichment and a corresponding volume loss of 90% was obtained (Figure 12b).

[33] 4. The inclination of the isocon line of the MSZ was 1.8 times greater than that of the HDZ, indicating a progressive enrichment toward the principal slip surface (Figure 12c).

5. Discussion

5.1. Mineralogical Trends Within the LFZ

5.1.1. Bulk Mineralogical Composition

[34] Combining the petrographic and mineralogical results (Figures 3 and 9), carbonate-rich protoliths are inferred for

both the ZJG and the PX exposures, at least for the fault core portions. At both locations, the inferred coseismic slip surface has cut through carbonate-bearing layers. Within the fault core, the content of carbonate minerals decreased notably toward the MSZ, whereas the content of quartz and clay increased. The feldspar content was relatively low (<3% for PX and <12% for ZJG exposure), showing a slight decrease toward the principal slip surface. The systematic decrease of carbonate mineral content toward the principal slip surface was the most distinctive characteristic of the transects studied. The corresponding reduction in carbonate mineral content normalized to the content at the margin of the fault core was ~76% and ~75% for the ZJG and PX exposures, respectively.

[35] At the PX exposure, fluid-derived minerals, such as gypsum, fluorapatite, and barite, were concentrated in the fault rock matrix at the fault core boundary (Figure 9), where white vein material also occurred, seemingly having been fractured after formation in situ by precipitation from the fault zone fluid. If this was the case, the vein material (consisting of 94% of dolomite and 5.2% of barite; Figure 9) should record information about the fluid composition. The matrix mineral assemblages of gypsum, fluorapatite, and barite suggest a typical low-temperature hydrothermal fluid [*Jacobsen et al.*, 1998]. By contrast, the vein material at the ZJG exposure is composed of 38% dolomite, 50% calcite, and 5% quartz (Figure 3) and is exceptionally rich in illite (ref. 30%) compared with nearby material (ref. ~9%). The widespread precipitation of dolomite suggests a fluid charged with high concentrations of Mg^{2+} at both exposures, whereas the enrichment in illite at ZJG can be interpreted as the product of hydrothermal alteration. This is also consistent with the observed enrichment in smectite content toward the slip surface in the fault core (Figures 3 and 9).

5.1.2. Clay Assemblage

[36] As shown by the XRD data for the gray and black gouges at both locations (Figure 13), these had quite different clay composition, although their bulk compositions were similar. Distinct characteristics of transformation from smectite to illite (PX exposure) or from I/S to illite (ZJG exposure) have been presented. Coseismic frictional heating has been previously proposed as a mechanism capable of producing these mineralogical changes toward illite. The following arguments support this illitization hypothesis (here, illitization is taken as a general concept involving reactions including dehydration, dehydroxylation of hydrated smectite, and the smectite-illite transformation): (1) the black gouge was identified associated the localized slip zone by field and microscopic analysis [*Han et al.*, 2010]. The color and very fine grain size suggested that it accommodated large displacement during the earthquake, just like the black gouge observed in the drilling core of the Chelungpu Fault [*Hirono et al.*, 2008]. (2) The black gouge was always thin (<7 mm in thickness). This implies high internal strain rate, favoring the frictional heating mechanism. (3) Except for slightly more quartz and less clay, the black gouge had similar mineralogical and chemical compositions to the gray gouge. Based on the reaction equation for illitization, smectite + (K^+, Al^{3+}) = illite + (Ca^{2+}, Mg^{2+}) + quartz + water [*Roland and Ola*, 1996], the products contain quartz. This reaction could therefore be responsible for the higher quartz content in the black gouge.
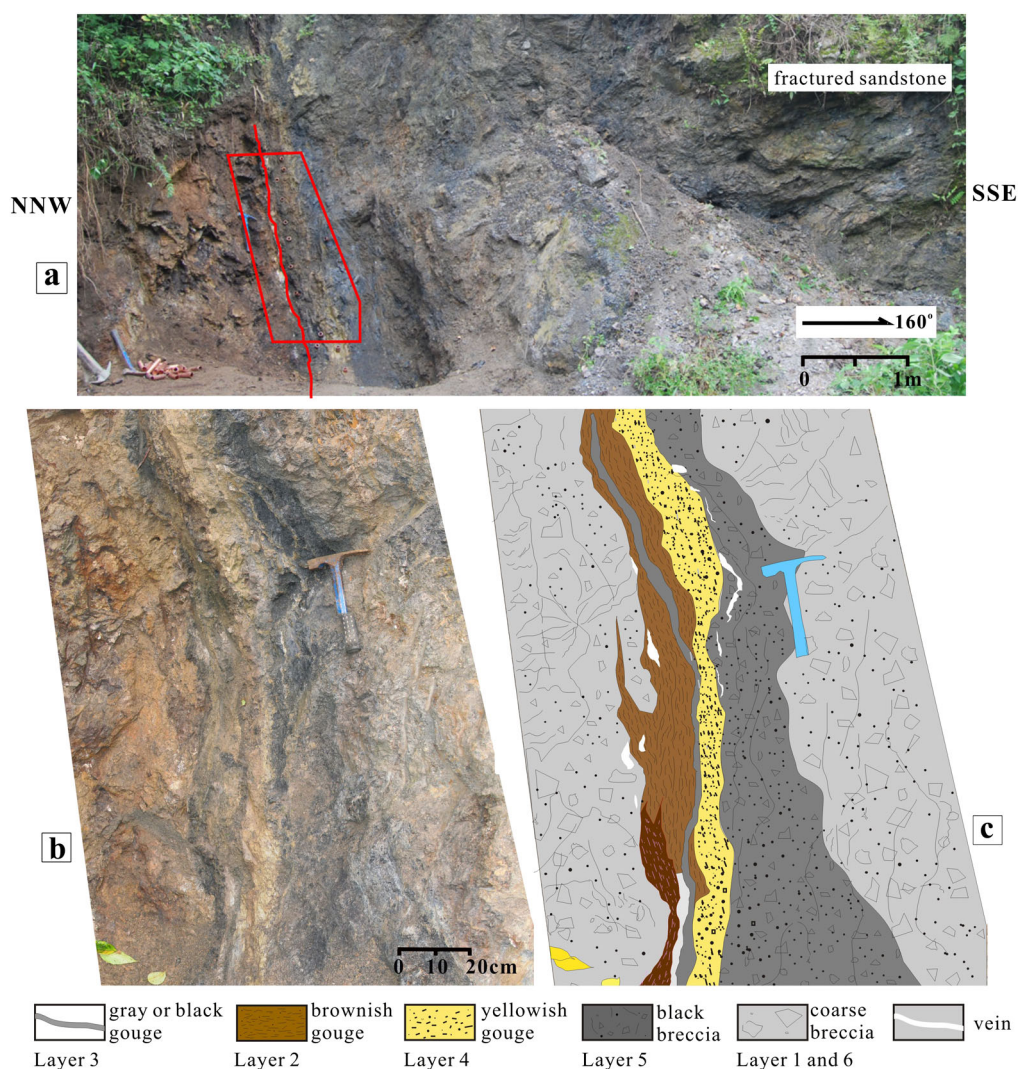
Figure 8. (a) Outcrop, (b) fault core structure, and (c) corresponding interpretive sketch of the PX exposure on the LFZ (GPS location is 32°17′14.63″N, 104°56′48.54″E).

(4) High-velocity frictional experiments on the PX fault gouge [*Yao et al.*, 2011] and on other smectite-rich gouge [*Ferri et al.*, 2010] have demonstrated that seismic slip can cause reduction in bulk clay content and in relative abundance of smectite. (5) Halloysite disappeared approaching the principal slip surface (Figure 9). Again, this is consistent with frictional heating, as discussed in Section 5.3. (6) A few additional measurements of magnetic susceptibility following *Yang et al.* [2012] showed that the magnetic susceptibility of the black gouge was 2.8–4 times higher than that of the gray gouge. The magnetic susceptibility values obtained are 13.13×10^{-8} m^3 kg^{-1} (black gouge) versus 4.68×10^{-8} m^3 kg^{-1} (gray gouge) for the ZJG exposure and 17.56×10^{-8} m^3 kg^{-1} (black gouge) versus 4.42×10^{-8} m^3 kg^{-1} (gray gouge) for the PX exposure, respectively. This may reflect the formation of ferrimagnetic minerals by thermal decomposition [*Tanikawa et al.*, 2007]. (7) The clay content data for the black gouges depart consistently from the overall profiles for the two transects studied (Figure 14). This suggests formation by a highly localized mechanism.

[37] Taken together, all seven arguments point to the black gouge's forming by illitization of the gray gouge. Despite this evidence, we cannot be certain that a coseismic smectite-illite transformation is the cause of the higher abundance of illite observed in the black gouge relative to the gray gouge. This is not only because the transformation involves chemical changes and is expected to be slow [*Huang et al.*, 1993] but also because dehydration or dehydroxylation can cause an apparent rise of illite content. In the coseismic decomposition model, the extent of reaction would be determined by the temperature rise during faulting and by the reaction kinetics. This information can be used to further test the model, as discussed in Section 5.3.

[38] Some further, general trends can also be inferred from the clay mineralogy of the transect samples. The results for both the PX and the ZJG exposures showed that the smectite and smectite-rich I/S contents gradually increase toward the principal slip surface. Illite behaved the opposite way, increasing in concentration away from the principal slip surface. The gray gouges showed the largest smectite or I/S content relative to the nearby samples (Figure 14), and at
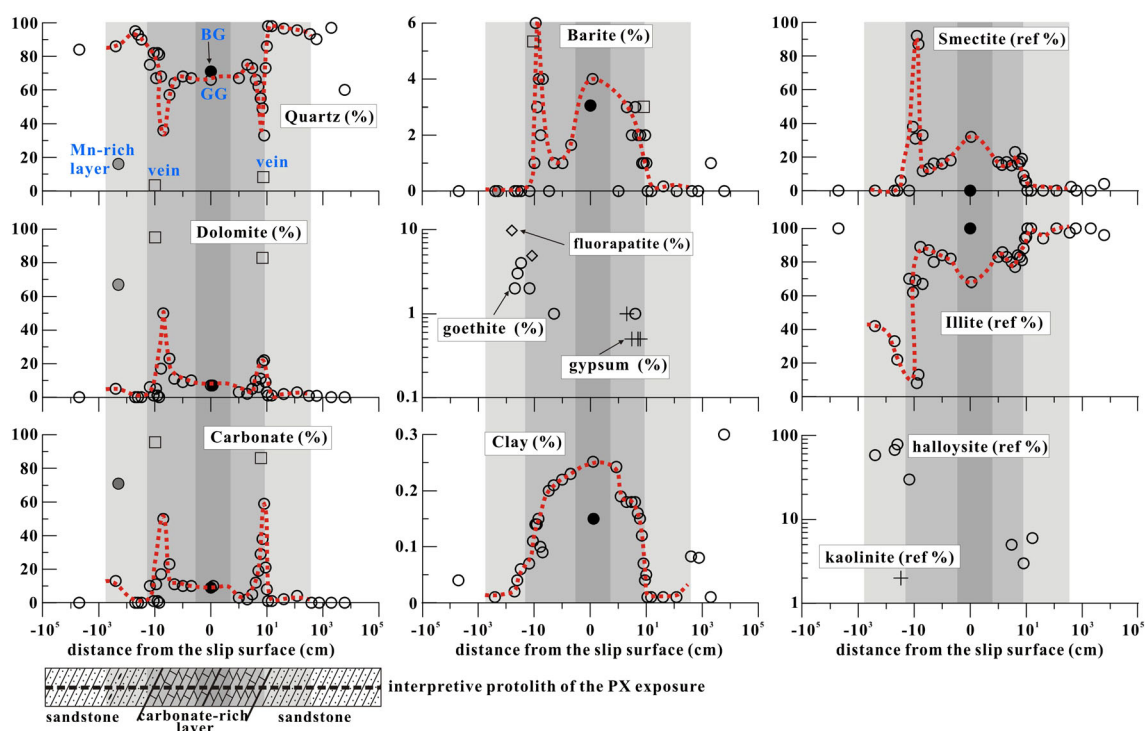
Figure 9. Variation in bulk and clay minerals (<2 μm) composition across the PX exposure. The squared symbols at the margins of the fault core represent the vein material. Solid circles stand for the Mn-ore layer on the hanging wall. Other detailed content as in Figure 3.

the ZJG exposure, the gray gouge showed the maximum value of S% (Figure 3). This smectite enrichment is consistent with that seen in gouge samples [*Xu and Li*, 2010] collected from ~600 m depth in the Wenchuan Fault Scientific Drilling project (WFSD; Borehole-1, located at the southern segment of the Yinxiu-Beichuan Fault, as shown in Figure 1). Therefore, although illitization occurred in the black gouge, the remainder of the fault core showed smectite enrichment. This observation indicates that the entire fault core underwent a retrograde reaction to form smectite.

[39] One explanation for this smectite enrichment is weathering [*Solum et al.*, 2003]. However, if weathering was responsible, the damage zone should be significantly affected too [*Isaacs et al.*, 2007]. The damage zone was heavily fractured and showed higher permeability [*Chen et al.*, 2011], hence likely provided a conduit for fluid flow. The brown color (Figure 8) and extensive deposition of supergenic minerals (Figure 9) consistently indicate surface leaching within the damage zone. The minerals formed include kaolinite and goethite, which are typical weathering products. However, although concentrated in the fine-grained fault center, little smectite formed in the damage zone. Moreover, smectite formation requires an interstitial fluid environment rich in Mg^{2+} [*Huang et al.*, 1993]. This cannot be supplied by the surface water. Finally, in preparing the exposures for sampling, more than enough surface material was removed to eliminate weathered rocks. Therefore, surface weathering alone does not seem to account for the distribution of smectite observed in the fault

rocks. Alteration of pseudotachylite has also been proposed as a mechanism of forming smectite in an active fault zone [*Kuo et al.*, 2009]. This is opposed by two arguments. One is that the enrichment of smectite affects the entire fault zone and that frictional heating could not produce such extensive melting. The other is that the fault core is rich in carbonate minerals (Figures 3 and 9), so that frictional heating would produce decomposition rather than melting.

[40] We propose that, in addition to limited weathering, fluid infiltration has played an active role in the transformation of the clay minerals present in the fault rocks in the shallow subsurface, especially in the postseismic stage. Smectite is a Mg-rich mineral that usually forms following the equation [*Roland and Ola*, 1996]: Mg-rich fluid + silicates → Mg-rich phyllosilicate assemblage. In our interpretation, the LFZ fluid was probably rich in Mg^{2+} as discussed in Section 5.1.1. Correlation analysis showed that the smectite content is correlated with an abundance of Ba. The profiles obtained for smectite and Ba are also similar, indicating that the formation of smectite may be related to the infiltration of hydrothermal fluid. Retrograde diagenesis of illite to smectite in sedimentary rocks induced by hydrothermal fluids has been well documented [*Zhao et al.*, 1999]. Similar observations and interpretations have also been reported for the Chelungpu thrust fault [*Isaacs et al.*, 2007]. Moreover, detailed geochemical evidence presented below indicates that the LFZ has experienced extensive hydrothermal fluid infiltration. We infer that frictional heating forming illite followed by the action of postseismic hydrothermal fluids controlled the mutual
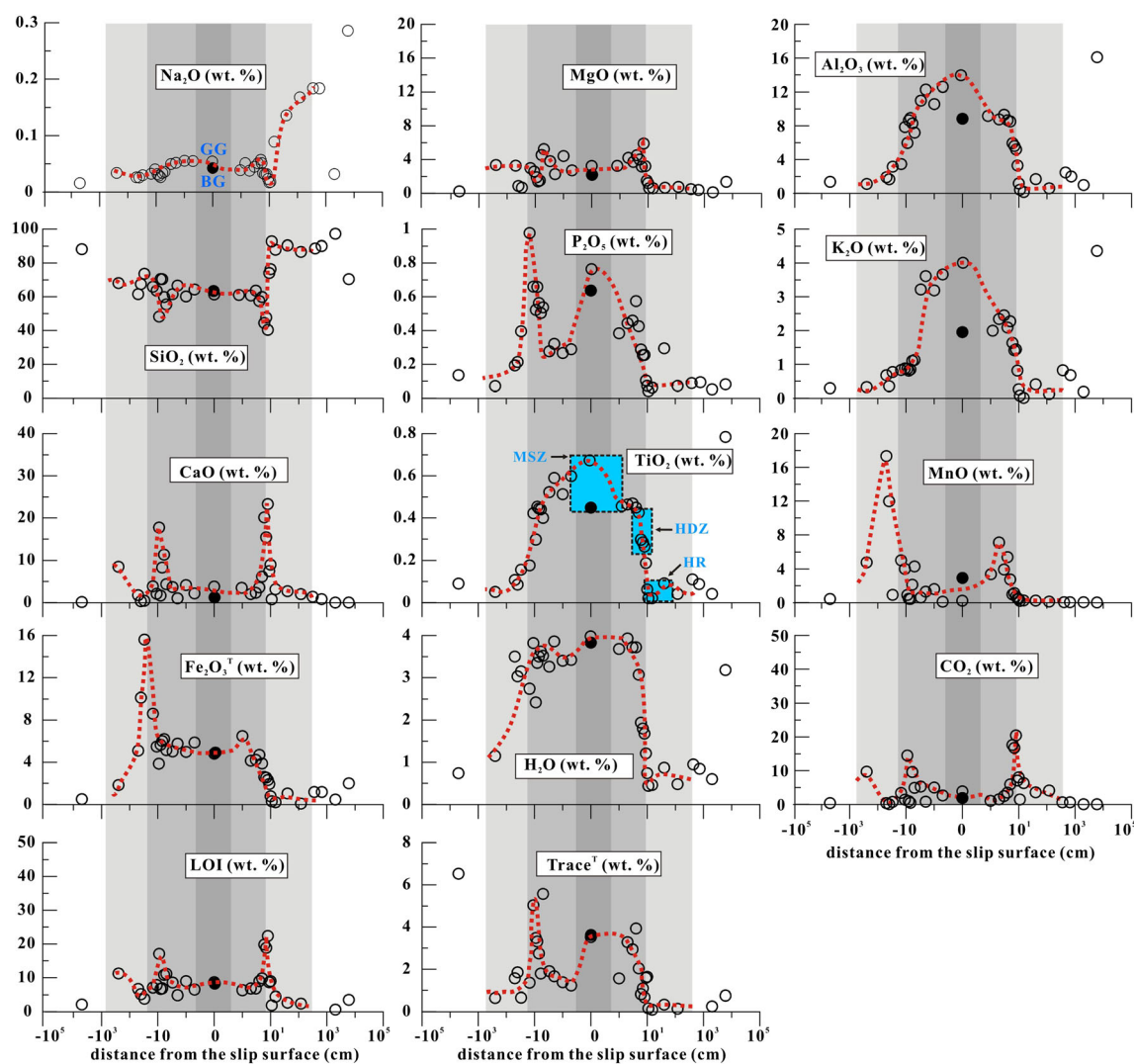
Figure 10. Concentration profiles of the bulk elements across the PX exposure. Detailed content as in Figure 4.

transformation between smectite and illite within the LFZ and the final abundances of these minerals.

5.2. Fluid Infiltration and Geochemical Trends Within the LFZ

5.2.1. General Geochemical Pattern and Volume Loss

[41] According to the transect variation profiles (Figures 4, 5, 10, and 11), the bulk and trace elements investigated can be classified into two broad types characterized by specific trends. The first is one of increasing depletion toward the principal slip surface compared with the HR (hereafter referred to as D-type). The second is one of systematic enrichment toward the principal slip surface (hereafter referred to as R-type). The relatively immobile, R-type major elements include Al_2O_3, K_2O, TiO_2, P_2O_5, $Fe_2O_3^T$, SiO_2, H_2O, and, to a lesser extent, Na_2O. Relatively mobile or D-type major elements include CaO, MgO, and CO_2, which are all carbonate-related oxides. MnO is not well categorized but more or less falls in the D-type category. Most trace elements showed immobile R-type behavior, except for Sr. Similar element classifications have been proposed previously [e.g., *Tanaka et al.*, 2001], but the

R- and D-type elements in our study are quite different from the classification employed for the granitic [*Goddard and Evans*, 1995] or clastic sedimentary fault zones [*Tanaka et al.*, 2001; *Chen et al.*, 2007], where depletion or enrichment corresponded the overall mobility of elements. It is well documented in these previous studies [*O'Hara*, 1988; *Goddard and Evans*, 1995; *Tanaka et al.*, 2001] that TiO_2, P_2O_5, MnO, and Zr are the most immobile oxides, followed by MgO, Al_2O_3, and V, and might therefore be expected to become enriched during geochemical alteration. By contrast, in the carbonate-rich fault zone investigated here, MgO and MnO fall into the mobile D-type category. Sr belongs to the D-type elements, because Sr^{2+} has an ionic radius of 112 pm close to that of Ca^{2+} (99 pm) and can easily replace Ca^{2+} in carbonate minerals.

[42] Summarizing, except for the carbonate-related outliers, the other elemental trends seen along the present transects exhibit increasing concentration toward the principal slip surface. This systematic variation suggests that a single process systematically controlled geochemical evolution. Combined with the petrographic and mineralogical trends (Figures 3 and 9), we propose that the geochemical trends seen
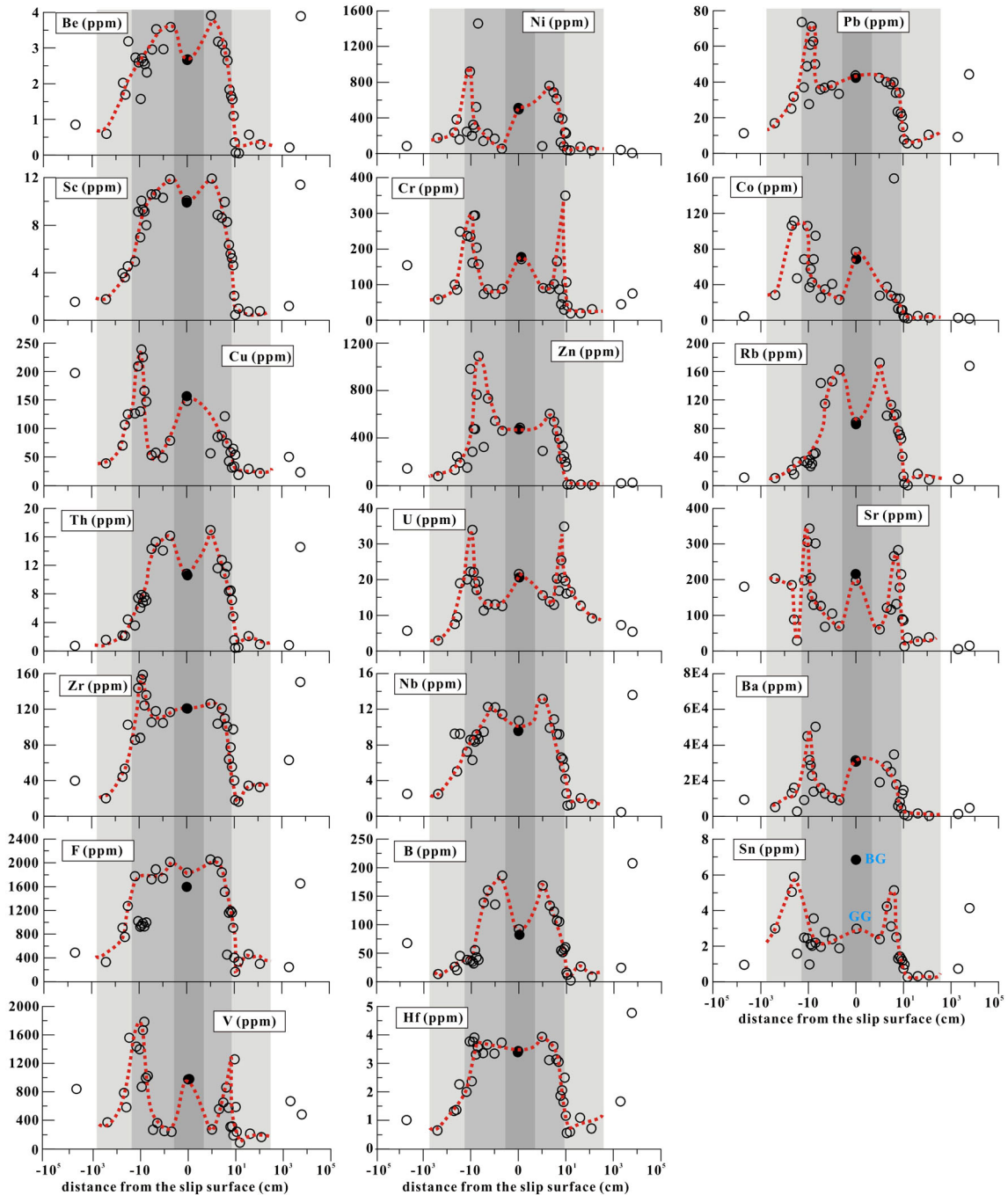
Figure 11. Concentration profiles of the trace elements across the PX exposure. Detailed content as in Figure 5.

in the LFZ (Figures 4, 5, 10, and 11) reflect the loss of carbonates and that the "mass removal" model may account for the observed enrichment signature. This idea is supported by both the correlation analysis and the isocon diagrams of Figures 6 and 12. The concentration of TiO_2 showed high correlation coefficients (typically >0.85) with R-type elements but negative correlation coefficients with D-type elements. The R-type elements, such as Al_2O_3, K_2O, SiO_2, and Fe_2O_3 for bulk elements and Be, Sc, K, Rb, Zr, U, Nb, Th, and Hf for trace elements, fall fairly close to the isocon line of TiO_2 at both the PX and the ZJG exposures (Figures 6 and 12). Conversely, the D-type elements were well below the isocon

line. Some elements exhibited an intermediate state, either reflecting their relatively high mobility (i.e., Na_2O) or perhaps an external contribution via deep fluid activity (i.e., P_2O_5, Ba, and F) or effects of adsorption by clay minerals (i.e., Cr and V).

[43] The isocon analysis further revealed that the volume loss at the ZJG and PX exposures was considerable (Figures 6 and 12). The values at the ZJG exposure were 87% for the HDZ and 93% for the MSZ. At the PX exposure, they were 83% for the HDZ and 90% for the MSZ. Assuming the unaltered fault core to have a homogenous geochemical composition, the carbonated-related elements (using CO_2 as the proxy and ignoring organic
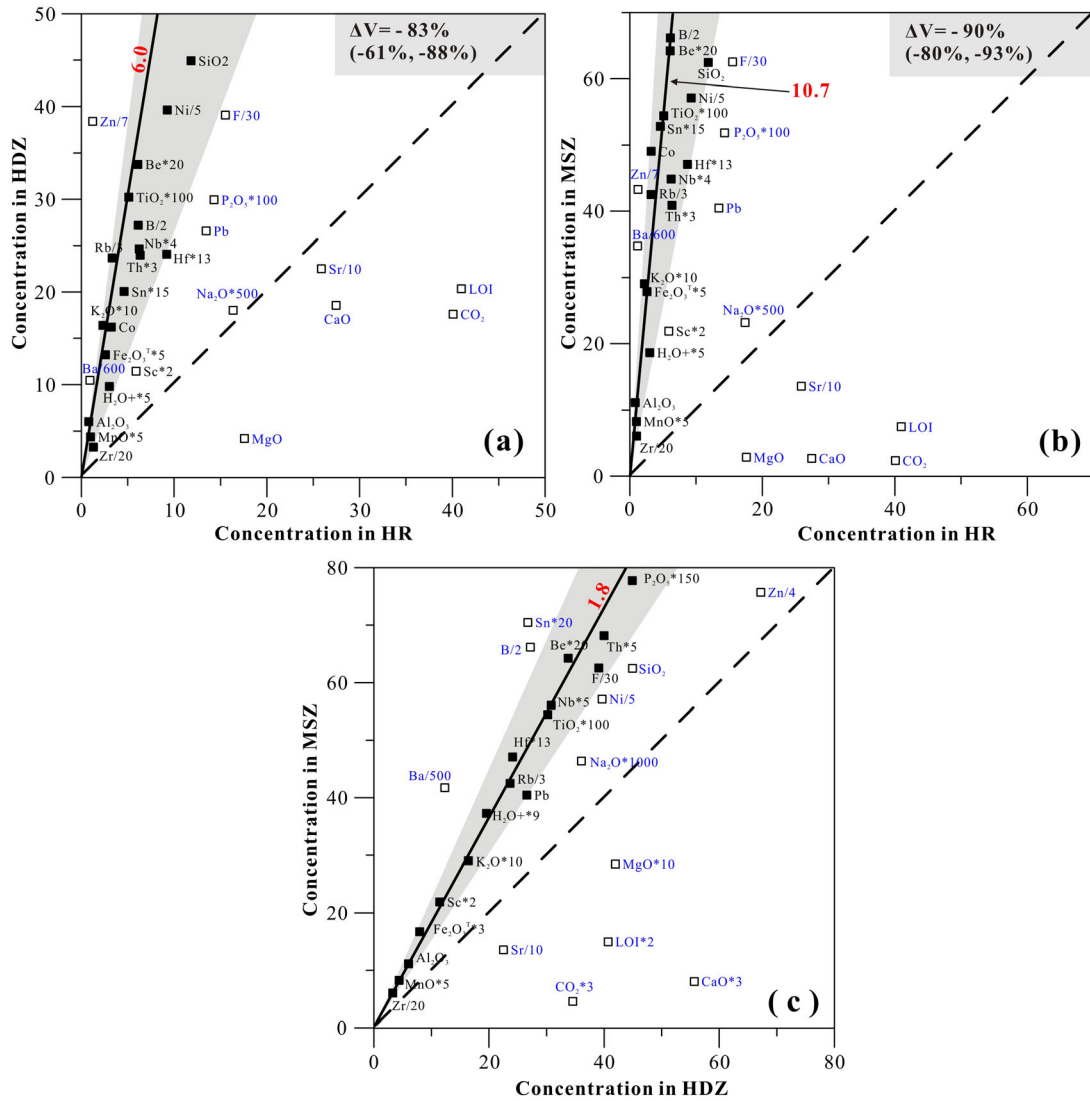
Figure 12. Grant-type plots for the HR against the HDZ and the MSZ as well as the HDZ against the MSZ at the PX exposure. Detailed content as in Figure 6.

carbon) exhibited an extreme depletion of ~80% for the ZJG exposure (Figure 4) and ~75% for the PX exposure (Figure 10), in agreement with the depletion degree in carbonate minerals of ~76% for the ZJG exposure (Figure 3) and ~75% for the PX exposure (Figure 9) as obtained in Section 5.1.1. On this basis, the overall volume loss from the LFZ portions studied, at least for the carbonate-rich segment, can be explained by the disappearance of carbonate minerals. The small discrepancy between the volume loss obtained by isocon analysis (Figures 6 and 12) and the depletion degree in carbonate-related elements (or minerals) may result either from introduction of mass through precipitation to form veins and cements or from decomposition of other minerals such as feldspar (Figure 3). The volume loss inferred in our study is much larger than that seen in previous studies of clastic-sedimentary [*Chen et al.*, 2007] or crystalline fault zone [*Tanaka et al.*, 2001]. In our study, especially for the fault core portion, the protoliths were carbonate rich. Carbonate minerals are less resistant to mechanical damage, and more susceptible to dissolution

and thermal decomposition, so that they can be easily disaggregated, dissolved, and transported away during long-term inter-seismic periods.

[44] Volume gain versus loss implies dilatational or compactional deformation of the zone affected. Based on the geochemically inferred volume loss of 80–90%, the LFZ must have therefore experienced major compaction. Taking the ZJG exposure for example, the width of the HDZ is ~18 cm (Figure 3), and the isocon analysis revealed a volume loss of ~87%, implying an initial zone thickness of 1.38 m (assuming constant density). Similarly, as the present thickness of the gouge zone is ~2 cm and the volume loss is ~93%, then the initial thickness should have been ~29 cm. Such large thickness changes are of major importance when estimation gouge surface energy and thermal pressurization associated with seismogenic faulting.

### 5.2.2. Mechanism of Mass Removal: Fluid Infiltration

[45] The bulk and trace element variation recorded along the PX and ZJG transects clearly indicates significant volume loss within the LFZ. There are three processes that

could account for marked reduction in carbonate mineral content: (1) thermal decomposition by frictional heating, (2) chemical dissolution, and (3) pressure solution under open-system condition. A reduction of inorganic carbon content has been reported for the principal slip zone of the Chelungpu Fault [*Hirono et al.*, 2006]. This was interpreted as due to thermal decomposition of the carbonate minerals through frictional heating at coseismic slip rates [*Han et al.*, 2007]. The higher magnetic susceptibility measured for the black gouge may also suggest formation of

ferrimagnetic material by thermal decomposition of iron-bearing dolomite (e.g., kutnohorite) [*Mishima et al.*, 2006]. In the present study, however, decarbonation is unlikely to have been the mechanism controlling volume loss, although it cannot be ruled out. Decarbonation is unlikely because frictional heating should be localized in a zone of finite width, rapidly decreasing away from the slip zone, and therefore failing to cause extensive decomposition. This is inconsistent with our stable isotopic data as discussed in Section 5.2.3.
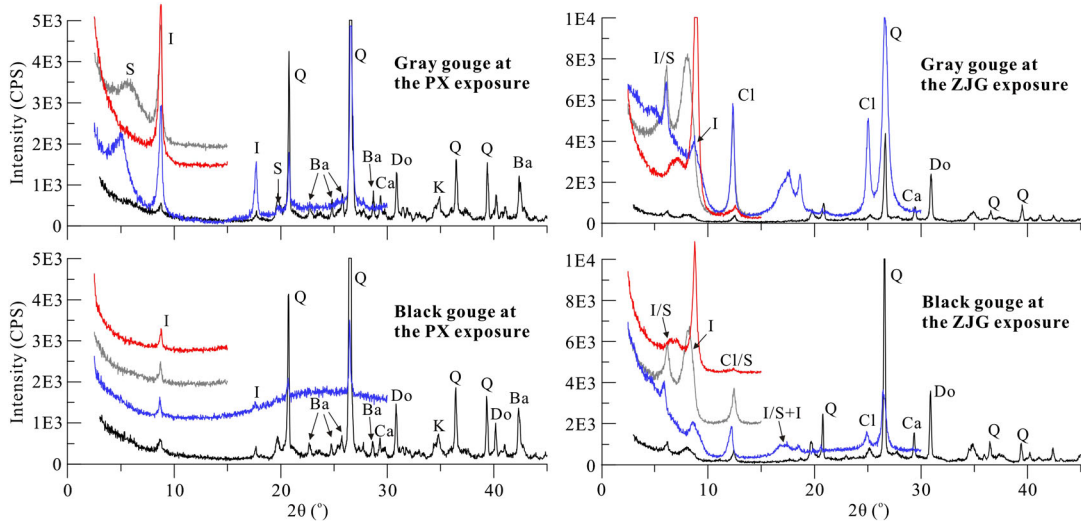
Figure 13. XRD patterns of the gray and black gouges of the PX and ZJG exposures for identifying the smectite to illite transition. Black lines are the results from the bulk powder samples. Gray, blue, and red lines are the results from air-dried, glycolated, and heated clay samples (<2 μm), respectively. Q, quartz; Do, dolomite; Ca, calcite; Ba, barite; K, K-feldspar; S, smectite; I, illite; Cl, chlorite; I/S, mixed layers of illite-smectite; Cl/S, mixed layers of chlorite-smectite.
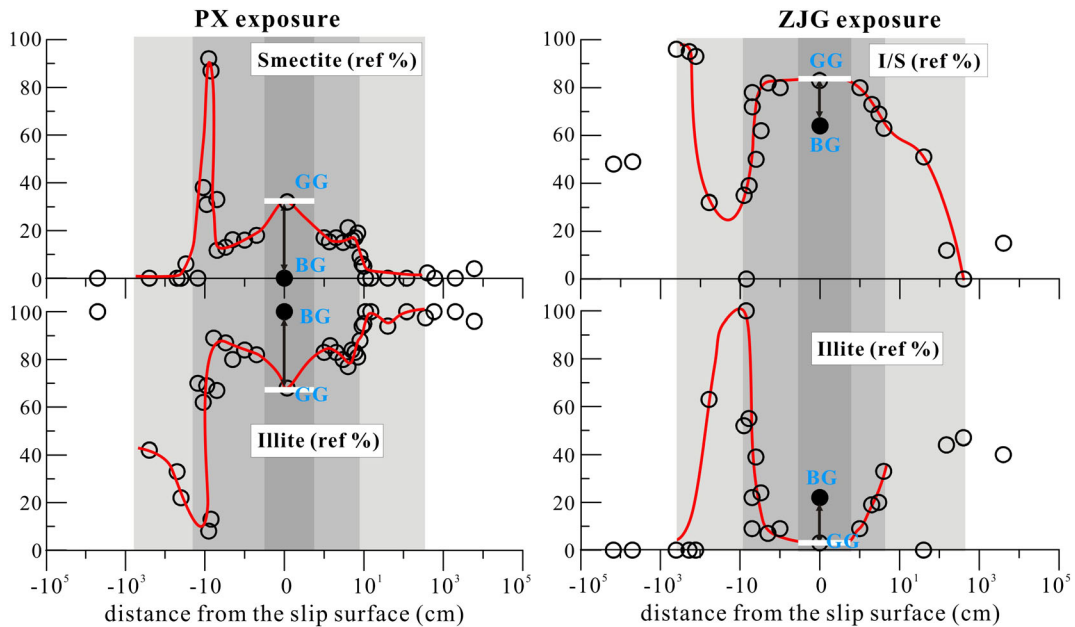
Figure 14. Concentration variations of smectite, illite, and I/S across the PX and ZJG exposure, showing the enrichment of smectite along the entire transect and the illitization in black gouge.

[46] If fluid infiltration occurred in the LFZ, chemical dissolution would be an important candidate mechanism for removal of carbonate minerals. Even though no pH data are available, on site fluid monitoring at the WFSD-1 and WFSD-2 drilling sites (Figure 1) has shown abnormal jumps in concentrations of CO_2 degassing from the fault zone following aftershocks [*Luo et al.*, 2010]. After the main Wenchuan Earthquake, the soil concentration of CO_2 also displayed conspicuous positive anomalies at several fault scarps along the LFZ [*Zhou et al.*, 2010]. On this basis, we infer a relatively acid pH for the interstitial fluid of the fault zone, perhaps facilitating the dissolution of carbonate minerals as the CO_2 pressure drops.

[47] Pressure solution is also an important mechanism in carbonate rocks [*Zhang, X., et al.*, 2010] and could be accelerated in the fault zone due to grain size reduction and/or fluid flow [cf. *de Meer and Spiers*, 1997]. Although negligible in the shallow subsurface, pressure solution may be significant at depth in the long-term interseismic phase. By examining the Grant-type plots (Figures 6 and 12), the MSZ displays larger inclinations than the HDZ, further implying that more mobile elements were lost from the slip zone than from the surrounding, highly damaged rocks. Grain size analysis revealed that the particle size of the fault rocks decreases toward the principal slip surface [*Chen et al.*, 2011]. The fine-grained signature of the slip gouge (with average particle diameter ~4 μm) suggests extremely high surface energy. This would increase the chemical potential hence solubility of the gouge by ~1–10 J/mol [$4\gamma\Omega/d$, where γ is interfacial energy (0.05–0.5 J/m^2), Ω is molar volume (~2×10^{-5} m^3/mol), and d is grain diameter], as well as increasing fluid-rock reaction rates, in proportion to the surface area. Accordingly, fluid-rock reactions (e.g., dissolution) within the MSZ should be much faster than in the HDZ. Moreover, pressure solution compaction and creep rates are inversely proportional to the particle size cubed (in the diffusion-controlled case, see *Zhang, X., et al.*, 2010). On this basis, we interpret the volume strain in the fault rocks to be associated with cataclasis during faulting and the subsequent fluid-rock interaction processes, including mass removal by chemical dissolution and likely compaction by pressure solution [*Gratier et al.*, 2011], although no direct evidence of pressure solution could be observed in these very fine grained materials.

[48] According to previous work [*Chen et al.*, 2011], the fault rocks of the PX and ZJG exposures display moderately high permeability (order of magnitude 10^{-16}–10^{-13} m^2) at effective pressures below 10 MPa, providing channels for easy fluid flow, which would further enhance fluid-rock reactions and mass removal by undersaturated fluids. On the contrary, the permeability of fault rocks is extremely sensitive to effective pressure so that it would decrease rapidly with increasing depth, implying reduced fluid flux and less mass loss at depth, unless fluid recharge from below could maintain high fluid pressure.

[49] It is important to note here that the volume changes that we report apply to portions of the fault zone that slipped repeatedly in the past. They are not coseismic volume changes but reflect accumulated mass and associated volume loss taking place over many previous earthquake cycles [*Zhang, P., et al.*, 2010]. Coseismic rupture can promote such mass removal processes by reducing the grain size

and increasing the surface area available for rock-water interaction. The cumulative nature of repeated slip events means that the material seen at the surface has been exhumed from deeper levels. Significantly, the present study area (Western Sichuan, China) is characterized by active uplift and erosion, an active hydrological system, and an extremely wet climate. Accordingly, most of the material that we infer was dissolved from fault zone would be easily transported away in both surface and groundwater.

[50] Generally speaking, fracturing, fluid infiltration, dissolution, and mass removal would result in a reduction of rock strength [*Sibson*, 1973] until (a) precipitation of strong mineral phases occurs, expanding the failure envelop [*Sibson et al.*, 1988; *Tenthorey et al.*, 2003; *Hausegger et al.*, 2010], or (b) compaction by pressure solution leads to gouge strengthening [e.g., *Yasuhara et al.*, 2005]. In this study, cementation and vein precipitation were well evidenced at both exposures. The fluid-related mineral phases dolomite, barite, gypsum, and fluorapatite were widely formed in the fault rocks. Microscopic examination showed different healing textures such as cross-cutting veins, aperture filling, and fragment cementation. Like dissolution, cementation and pressure solution are also interfacial processes that are accelerated in fine-grained materials with high surface area. This may explain why cemented ultracataclasite occurs adjacent to the MSZ at the ZJG exposure (Figure 2b).

5.2.3. $\delta^{13}C$-$\delta^{18}O$ Distribution and Related Modeling

[51] Stable isotope geochemistry provides hints on the origin of the fluid, the water-rock ratio, and fluid-rock interaction along fault zones [*Molli et al.*, 2010]. The distinct differences in $\delta^{13}C$ values observed between the fragments, matrix, and veins material in our study (Figure 7) suggests that the source of the inorganic carbon cannot be attributed just to remobilization of normal marine sedimentary carbonate (i.e., protolith) whose $\delta^{13}C$ values are approximately −2% (Figure 7). With respect to the limestone country rock, matrix and vein material within the fault core studied were depleted in heavy isotopes such as ^{13}C. This is expected to result principally from interaction with external fluids depleted in ^{13}C and ^{18}O [*Wang et al.*, 2010] or from other processes such as thermal decomposition [*Shieh and Taylor*, 1969].

[52] According to high-velocity frictional experiments, thermal decomposition of carbonate minerals by frictional heating may be a common phenomenon in natural faulting [*Hirono et al.*, 2006], which could produce significant dynamic weakening [*Han et al.*, 2007]. Decomposition leads to the production of CO_2 enriched in heavy ^{13}C and ^{18}O, thus lowering the heavy isotope content of the residual carbonate minerals [e.g., *De Paola et al.*, 2011]. Because most samples subjected to isotopic analysis in this study were collected from the fault core, they may have experienced high temperatures, hence decomposition and related isotopic fractionation effects. Using large breccia fragments (>5 mm, $\delta^{13}C = -1.9‰$ and $\delta^{18}O = 26.2‰$) as an approximation of initial protolith material, isotopic fractionation by thermal decomposition was calculated following the fractionation equation for a closed system, written as $\delta_f = \delta_i + 1000(F - 1)\ln(\alpha)$, where i and f denote the initial and final composition, F is the residual component, and α is the fractionation factor [*Sheppard and Schwarcz*, 1970].

The results for 400°C and 600°C (Figure 15) indicate that the fractionation trend for pure decarbonation cannot fully explain the observed evolutional trends, so that alternatives should be explored.

[53] If fluid entering the fault zone is assumed to have had constant isotopic composition [*Hausegger et al.*, 2010; *Molli et al.*, 2010], the relative position of individual data points in the $\delta^{13}C$–$\delta^{18}O$ diagram (Figure 7) may relate to variations in the amount of fluid interacting with the sample [*Kirschner and Kennedy*, 2001; *Pili et al.*, 2002, 2011]. Large breccia fragments with isotopic values near the protolith interacted with small quantities of fluid. Matrix and vein material with more depleted isotopic values either interacted with larger quantities of fluid or precipitated from a fluid that had partly retained its original isotopic values. Overall, the isotopic discrepancy between fragments, matrix, and vein material may be explained by a model in which (1) external fluids were involved in the vein precipitation and matrix cementation, and the most ^{13}C-depleted values shown by sparry dolomite adjacent to the principal slip surface reflect their proximity to the hydrocarbon source ($\delta^{13}C = -8.0‰$ and $\delta^{18}O = -11.5‰$), and (2) the precipitating fluid interacted with the breccia fragments modifying its original isotopic composition. There are several candidate origins of fluid depleted in ^{13}C. The first is related to organic complexes, which could evolve to yield strongly negative $\delta^{13}C$ values [e.g., $-27.6‰$ in *Hellings et al.*, 1999]. However, there is no evidence for organic fluid activity near the ZJG exposure. The second is the contribution of mantle-derived carbon

dioxide with $\delta^{13}C \approx -5‰$ [e.g., *Ballentine and O'Nions*, 1994]. This seems unlikely as no mantle-derived features were recognized, and the $\delta^{13}C$ values measured were more negative. The third and most likely possibility is fluid of meteoric origin.

[54] Assuming the veins crystallized from meteoric fluid after reacting exchange equilibrium with the surrounding breccia fragments, mass balance modeling of the isotopic composition of the matrix and vein material can be carried out. At the fluid-fragment interface, cation exchange may take place providing calcium to the solution and promoting equilibrium with respect to the vein material. This means that the ^{13}C and ^{18}O content of veins precipitated from the fluid would be principally determined by differences between the isotopic composition of fluid and that of breccia fragments. Following the mass balance approach by *Zheng and Hoefs* [1993], the governing equations for calculating the ^{13}C and ^{18}O content of vein material precipitated from a fluid after interaction with the fragments, assuming bicarbonate (HCO_3) as the dominant carrier of carbon in the fluid, are

$$\delta^{13}C^f_{vein} = \delta^{13}C^i_{HCO_3} + 1000\ln\alpha^{vein}_{HCO_3} + \gamma^{-1}\left(\delta^{13}C^i_{frag} - \delta^{13}C^f_{frag}\right) \quad (1)$$

$$\delta^{18}O^f_{vein} = \delta^{18}O^i_{H_2O} + 1000\ln\alpha^{vein}_{H_2O} + \gamma^{-1}\left(\delta^{18}O^i_{frag} - \delta^{18}O^f_{frag}\right) \quad (2)$$

[55] Here, i and f denote the initial and final composition, α is the fractionation factor, and γ is the water-to-rock ratio. In these calculations, we assumed a typical meteoric water composition with $\delta^{13}C^i_{HCO_3}$ of $-12‰$ and $\delta^{18}O^i_{H_2O}$ of $-7‰$. We also assumed a fluid temperature of 70°C. The fractionation factors are 1.4‰ for $\delta^{13}C$ of HCO_3-$CaCO_3$ [*Ohomoto and Rye*, 1979] and 20.7‰ for $\delta^{18}O$ of H_2O-$CaCO_3$ [*O'Neil et al.*, 1969]. The ranges in isotopic composition in exchanged fragments were 2.1‰ for ($\delta^{13}C^i_{frag} - \delta^{13}C^f_{frag}$) and 4.5–6.0‰ for ($\delta^{18}O^i_{frag} - \delta^{18}O^f_{frag}$) (Figure 7). As shown in the calculation results presented in Figure 15, the model for interaction between breccia and meteoric water can account for the isotopic data characterizing the matrix and vein material. The modeling also indicates water-to-rock ratio in the range of 0.15–0.20 (Figure 7), corresponding to 75–100 g water/kg breccia.

[56] We infer that the ^{13}C-depleted carbonate veins and cements, as well as other fluid-related minerals such as barite found in the two sections of fault zone studied, were probably formed at the postseismic stage, when deep fluid with excess pressure rose up and interacted with the fault rocks along the fault plane. During this period, healing processes, and the resulting impermeable barrier formed from cemented fault gouge and HR [*Chen et al.*, 2011], caused a gradual pressure increase in pore fluid entrapped in the damage zone at depth. This led to subsequent frictional failure and the development of a temporarily open system accessible for fluid flow. This alteration between brittle failure and cementation implies a cyclic change between an open and a closed fault zone system, that is, fault valve behavior [c.f., *Sibson*, 1990].
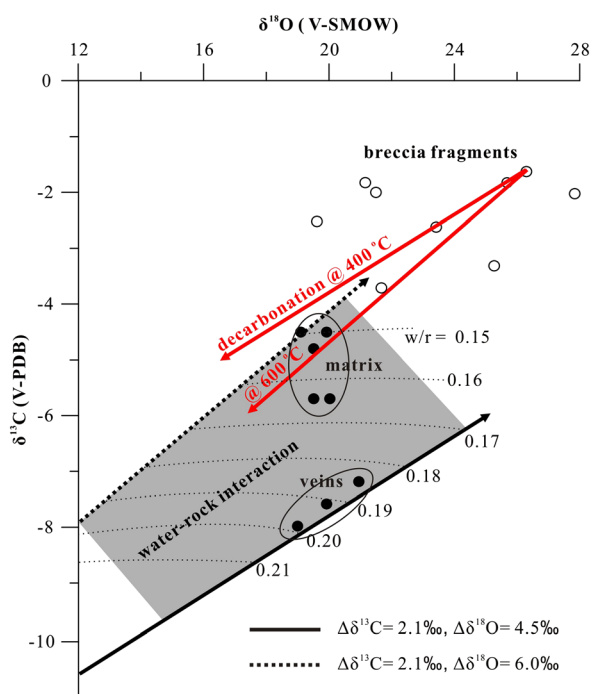
Figure 15. Modeling of $\delta^{13}C$ versus $\delta^{18}O$ values obtained from isotopic analyses of the ZJG exposure. The red lines are predicted by theoretical fractionation for decarbonation at 400°C and 600°C. The black lines are the calculated results assuming the vein and partially the matrix material were crystallized from the fluid after exchange equilibrium with the breccia fragments. Other detailed content as in text.

5.3. Clay Mineral Transitions in the Fault Gouge and Their Dynamic Effects

[57] The gradual enrichment of smectite (or smectite-rich I/S) toward the principal slip surface, along with the illitization in the black gouge seen in both study exposures, implies that we should be able to obtain useful information about the faulting mechanism from the in situ clay mineralogy. Although the smectite-bearing upper portion of the LFZ was passively displaced and did not radiate seismic energy, it provides a good illustration of the transition from illite (or illite-rich I/S) to smectite (or smectite-rich I/S) in an active fault zone. This is important for discussing the slip stability of a fault zone containing clayey-gouge [*Brace and Byerlee*, 1966]. Smectite is a mineral with one of the lowest coefficients of friction and is usually regarded as an important contributor to coseismic slip weakening [e.g., *Lockner et al.*, 2011]. In addition, the frictional resistance could be further lowered by the introduction of water produced locally by coseismic dehydration of smectite as discussed below.

[58] Coseismic decomposition reactions, such as dehydration of serpentine, kaolinite, and smectite, have been previously demonstrated in both experiments [*Hirose and Bystricky*, 2007; *Brantut et al.*, 2008; *Ferri et al.*, 2010] and fieldwork [*Hirono et al.*, 2007, 2008; *Hamada et al.*, 2009]. For example, *Hirono et al.* [2008] analyzed the clay composition of the Chi-chi earthquake cores and found that the kaolinite and smectite contents were lower in the black gouge than in the surrounding rocks. The dewatering process might have significantly affected the faulting mechanism, because these clay minerals can release water, lowering the fault strength rapidly. In our study, although to a limited extent, illitization has occurred in the black gouges even at the surface. At low pressure condition, smectite begins to lose interlayer water at 110°C and illite starts to form at temperatures above ~150°C [*Saffer and Marone*, 2003]. A simple order of magnitude calculation shows that, at or just below the ground surface, normal stresses are too low to produce enough frictional heat to transform smectite into illite. A first possibility we offer to explain the observed illitization is that irregularities in the slip surface caused high local normal stress and thus irregular, increased heat production along the slip surface. This is consistent with the discontinuous nature of the black illitized gouge. The second possibility is that coseismic slip was highly localized. This is probably the reason why illitization only occurred to the thin black layers. An additional possibility is that drastic grain size reduction or comminution within the fault rocks promoted illitization by means of water expulsion and chemical exchange, the reaction kinetics of which are poorly known for nanoparticles. We speculate that illitization may become increasingly important at depth because of increased frictional heating, if other factors remain unchanged [*Huang et al.*, 1993]. According to the chemical formula of typical smectite ([Ca$_{1/2}$,Na]$_{0.35}$[Al,Mg]$_2$Si$_4$O$_{10}$[OH]$_2$ · nH$_2$O, where n is the number of moles of water in 1 mole smectite) and illite ([K,H$_3$O]Al$_2$Si$_3$AlO$_{10}$[OH]$_2$), the reaction products of smectite-illite transformation are aqueous silica, Mg^{2+} and water, via the following reaction [*Roland and Ola*, 1996], smectite + feldspar (or pore water) = illite + quartz (or chlorite) + water + cations. The released silica and Mg^{2+} charged pore fluids might migrate along the fault zone during coseismic dilatation [*Goddard and Evans*, 1995] and/or via fault-valve action [*Sibson*, 1990], flushing the fault zone near the surface, promoting new smectite formation at higher levels. Therefore, a self-enhancing feedback mechanism is proposed to explain the features demonstrated above, namely, the Mg-rich fluid and the enrichment in smectite.

[59] According to the reaction equation, illitization of smectite involves liberation of a large quantity of water either interlayer water or structural sites. However, a solid volume reduction of 33–47% is also involved because the lattice structure collapses from 150–190 to 100 nm [*Vrolijk and van der Pluijm*, 1999]. These two aspects counteract each other in terms of pore pressure change. Synchrotron studies showed that the temperature for smectite dehydration increases with increasing pore pressure [*Huang et al.*, 1994]. The positive Clausius-Clapeyron coefficient indicates that the total volume of reaction products was larger than that of the reactants. In addition, the interlayer water is denser than that of the pore fluid [*Hawkins and Egelstaff*, 1980]. Taken together, most available evidence favors pore pressure increase during the smectite-illite transformation. Based on this idea, we now carry out calculations to estimate the influence of this dewatering process, induced by frictional heating, on the faulting behavior of the Wenchuan Earthquake.

[60] With increasing depth, the higher normal stress should produce more frictional heating. Modeling work on heat production during the Wenchuan Earthquake predicts a peak temperature of 600°C, with an average temperature of 400°C lasting for >150 s at 600 m depth [*Yang et al.*, 2012]. In terms of reaction kinetics, dehydration of smectite is very fast, occurring on a timescale of minutes [*Huang et al.*, 1994; *Hirono et al.*, 2008]. Assuming the same clay composition as analyzed on the surface, we can estimate the amount of water expelled from the gouge and the possible effect on generating excess pore pressure at 3 km depth during the Wenchuan Earthquake. Assuming 1 mol hydrated smectite converts to 1 mol dehydrated material, losing χ mol water and producing a volume reduction of the solid phase of ΔV, the potential pore pressure increment induced by the reaction can be expressed as follows:

$$\Delta p = \lambda(1 - \phi)\left(\frac{\chi M_{H_2O}}{M_{hy}}\frac{\rho_s}{\rho_f} - \Delta V\right)/S_s, \qquad (3)$$

where λ is mass percentage of hydrated smectite in the gouge, ϕ and S_s denote porosity and specific storage (Pa^{-1}) of the fault gouge, χ is the number of moles of water released from 1 mole smectite, M_{H_2O} and M_{hy} are the molar masses of water (18 g/mol) and smectite (366 + n × 18 g/mol), and ρ_f and ρ_s are densities of fluid (1.0 × 10^3 kg/m^3) and solid phases (2.61 × 10^3 kg/m^3). This formula is similar to Equation (15) given by *Brantut et al.* [2010]. The term $\Gamma = \frac{\chi M_{H_2O}}{M_{hy}}\frac{\rho_s}{\rho_f} - \Delta V$, defined as specific expelled water, is a general expression. For a given dehydration reaction, Γ is a constant, representing the amount of water (vol.%) released. If ΔV is large enough, Γ would be zero. This corresponds to the case in which the overpressure induced by fluid production is compensated by the porosity increase induced by lattice collapse.

[61] In the following, a fully hydrated smectite with three interlayers of water are initially assumed. The cases of losing one, two, and three interlayers of water are then explored. The number of moles of water contained in per mole of smectite with one, two, and three interlayers of water are 1.9, 4.5, and 7.16, respectively [*Liu and Lin*, 2005]. These figures imply that the χ values associated with losing one, two, and three interlayers of water are 2.66, 5.26, and 7.16, respectively. ΔV can be estimated by considering change of basal spacing (d_{001}) for smectite transferring from one hydration state to another. Smectite has four discrete d_{001} corresponding to its four states, that is, 100 nm for the fully dehydrated state versus 124, 156, and 188 nm for the hydrated states with one, two, and three interlayers of water [*Huang et al.*, 1994 and references therein]. This yields ΔV values of 17.0%, 34.0%, and 46.8% associated with releasing one, two, and three interlayers of water. Substituting the appropriate values of χ and ΔV into the expression above for Γ gives specific expelled water as 8.2%, 15.9%, and 21.2%, respectively. The mass content of smectite (λ) can be calculated from the mineralogical results (Table 2). In situ porosity (ϕ) and specific storage (S_s) measured on core samples in laboratory were also applied (Table 2).

[62] The calculation showed that losing one interlayer of water in smectite generates ~6.5 MPa excess pore pressure over the hydrostatic head at 3 km depth (Table 2). This value can increase to 17.5 MPa if the smectite interlayers are fully dehydrated. Such behavior will cause a reduction in effective normal stress acting on the fault plane from 45 to ~27.5 MPa. Indeed, our calculation should underestimate the dynamic weakening effect that actually occurred in the Wenchuan Earthquake because thermal pressurization is not taken into consideration. On the contrary, the dehydration of smectite is an endothermic reaction [*Hirono et al.*, 2008]. Hence, there is a temperature decrease effect during the reaction. Hence, there is consumption of thermal energy during the reaction, which in turn limits the temperature and pore pressure increase. Alongside thermal pressurization, however, this effect is expected to relatively small compared with that of the released of interlayer water. To explore the coseismic thermal-mechanical-chemical process in more detail, numerical modeling coupling the kinetic process of chemical reaction with frictional heating and fluid transportation is needed in the future [*Sulem and Famin*, 2009; *Brantut et al.*, 2010].

[63] A similar treatment to the above can be applied for halloysite, which is concentrated at the margins of the fault core (with maximum content of 3.1 wt.%) while being absent from the slip zone (Figure 9). Halloysite has nearly the same chemical composition ($Al_4[Si_4O_{10}][OH]_8 \cdot nH_2O$) as kaolinite but contains water interlayers. In terms of lattice structure, kaolinite consists of layers of Si-O tetrahedra and Al-(OH) plates linked by hydrogen bonds, whereas, in halloysite, the existence of interlayer water destroys the hydrogen bond, so that the Si-O tetrahedra and Al-(OH) plates must bend to accommodate the change in unit cell dimensions, thus developing a curled or tubular shape. Halloysite therefore forms a natural nanoparticulate material, and at 50–90°C, it dehydrates to kaolinite [*Brindley*, 1952]. Considering it is too unstable to survive at depth, we did not take its dehydration into account in our calculation. At shallow depths, however, its dynamic effect on faulting would be considerable as it decomposes at low temperature and the reaction rate is expected to be fast because of the nanoparticle size. Furthermore, other reactions such as the dehydration of gypsum could also occur but are not included here considering the low content of such phases (Figure 9). Finally, we should point out that whether these dewatering reactions occurs or not depends on whether the fault system is drained or undrained. Under drained conditions, although dehydration can easily occur, the system is relatively open so that excess pore pressure is unlikely to be generated during faulting. By contrast, under undrained or partially drained conditions, dehydration reactions may be prohibited and the effect of dewatering will depend strongly on the transport properties (i.e., permeability and specific storage) of the gouge samples.

5.4. Implications for Subsurface Processes

[64] We will now apply our interpretations of the processes that operated at the two surface exposures studied to construct an integrated, conceptual model synthesizing the coupling between fault activity, fluid migration, mass transport, and geochemical evolution that can occur under near-surface conditions in active carbonate fault zones. We assume that the processes inferred at the surface will also occur in the subsurface and reason to what depth they may extend. Our model is represented in Figure 16. It assumes cumulative carbonate removal as a key process so is limited to carbonate-bearing systems. It incorporates the following feathers.

[65] First, the efficiency of carbonate removal is determined by dissolution and advective transport, probably enhanced by pressure solution, especially in compressional

Table 2. Estimation of the Amount of Water Expelled by Dehydration of Interlayer Water in Smectite[a] and the Dynamic Effect on Generating Excess Pore Pressure[b]

Principal slip gouge	ZJG gray gouge	PX gray gouge
Clay content of bulk sample (wt.%)	34	25
Reference content of smectite (%)	31.5	32
Smectite content (wt.%)	10.7	8.0
Porosity (%) at 3 km	12.8	10.7
Specific storage (Pa^{-1}) at 3 km	1.2×10^{-9}	8.1×10^{-10}
ΔP_f (MPa) by losing 1 layer of H_2O	6.3	7.2
ΔP_f (MPa) by losing 2 layers of H_2O	12.4	14.0
ΔP_f (MPa) by losing 3 layers of H_2O	16.5	18.7

[a]Smectite here includes pure smectite and smectite contain in I/S. The reference content of smectite in I/S is equal to the reference content of I/S multiplied by S%.

[b]Calculations were conducted at 3 km depth under an effective pressure of 45 MPa.
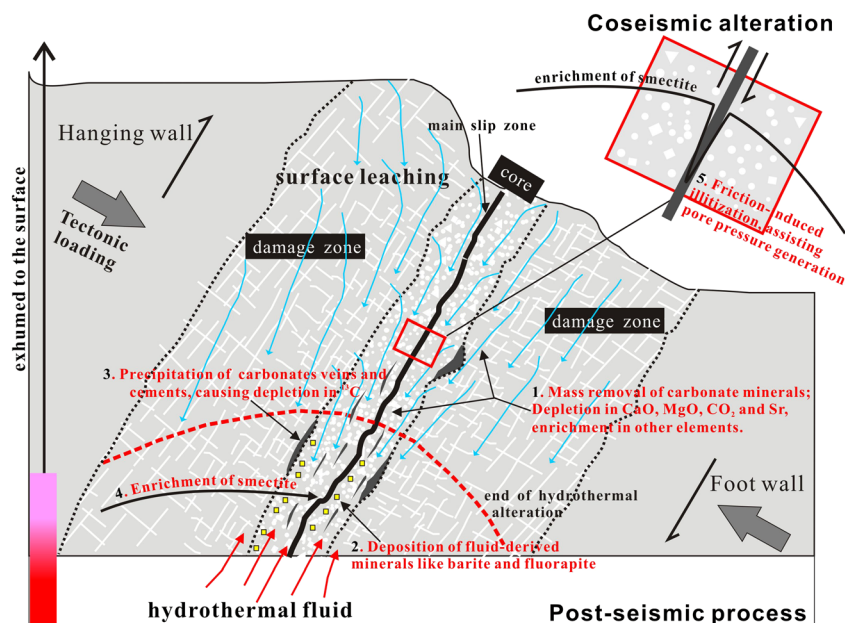
Figure 16. Integrated conceptual model illustrating the complete set of mechanochemical processes inferred to affect the geochemical evolution of the carbonate-rich fault zones studied here and perhaps more generally. Note the five key features of the model.

tectonic settings. Although the solubility and dissolution rate of carbonate are relatively insensitive to temperature [*Zhang, X., et al.*, 2010], at depths greater than 2.5–5 km, porosity and permeability of both fault core and surrounding rock will become strongly reduced due to elevated effective stress [*Wibberley and Shimamoto*, 2003] and thermally activated compaction/healing processes [*Tenthorey et al.*, 2003]. This will limit the advective mass removal process. The implication is that the cumulative volume/mass removal phenomenon reported here, and schematically illustrated in Figure 16, will only be important in the upper few kilometers of the crust, where groundwater movement can affect the fault zone. The second feature of our model is cyclic upwelling of hydrothermal fluids originating at depth, notably in postseismic periods when the fault valve is temporarily opened [*Sibson*, 1990]. This results in extensive deposition of characteristic minerals such as barite and fluorapatite. Third, hydrothermal fluid probably of recirculated meteoric origin leads to precipitation of carbonate veins and cements, resulting in the observed depletion of ^{13}C in the carbonate-hosted fragments. Fourth, the various cycles of the hydrothermal alteration cause increasing enrichment of smectite toward the principal slip surface. Last, the inferred process of smectite illitization and release of interlayer water by coseismic frictional heating, modified by thermal pressurization and endothermic dehydration reaction, cyclically modifies the principal slip gouges. This process will of course be limited to the upper 2–3 km of the crust where temperatures are low enough for smectite to form in the first place. With increasing depth, the coseismic temperature rise driving the illitization reaction; hence, the extent of illitization can be expected to increase also, because the higher normal stress should produce more frictional heating. The released fluid may be capable of increasing fluid pressure sufficiently to significantly enhance dynamic rupture propagation.

[66] One key point about this model should be emphasized further. Ongoing activity of the hydrothermal processes involved (items 2–4 in Figure 16) should be limited by reactant supply on the one hand and by the healing and sealing of fault permeability on the other. However, paleoseismic studies [*Zhang, P., et al.*, 2010] have revealed that many previous earthquakes have occurred along the LFZ. The active uplift and erosion going on in this area accordingly implies that the material seen at the surface now has been exhumed from the subsurface. It is the cumulative nature of repeated seismic events that explains the large volume loss observed at the sites that we studied. Our model predicts that similar effects should occur in other active, carbonate-bearing fault zones too.

6. Conclusions

[67] The main conclusions of this study of the ZJG and PX sites on the LFZ are summarized below.

[68] 1. Mineralogical and geochemical profiles along with the isocon diagrams, as well as isotopic results, consistently demonstrate that pervasive fluid infiltration occurred and altered the chemical architecture of the carbonate-dominated fault zones. Enrichment/depletion patterns, elements partitioning, and the large volume loss characterizing the carbonate-rich fault zones investigated are quite different from those characterizing granitic and clastic sedimentary fault zones. A mass removal model, involving dissolution and transportation, likely enhanced by pressure solution creep, is accordingly proposed and can account for the signatures observed in the carbonate-rich fault zone studied.

[69] 2. The increasing enrichment in smectite toward the slip surface, the high abundance of fluid-related minerals and elements, as well as the depletion in heavy isotopes (^{13}C) recognized in the fault zones studied consistently

suggest activity of fluids of hydrothermal origin. Faulting and cementation by deep fluids played a fundamental role in the evolution of the fault zone, with a cyclic change between an open and a closed permeability system during fault evolution. Stable isotope compositions (δ^{13}C and δ^{18}O) indicate continuous equilibration between protolith-derived breccia fragments and vein material (or cements) precipitated from fluids.

[70] 3. The black gouge found in the studied exposures on the LFZ is inferred to be the material having accommodated most of the displacement during the Wenchuan Earthquake. Illitization caused by frictional heating has occurred within it. We propose that frictional heating effects along with the action of postseismic hydrothermal fluids controlled the transformation and distribution of smectite and illite within the fault core of the LFZ. The dehydration of smectite by frictional heating is expected to have been most extensive at depth. Numerical modeling indicates that excess pore pressures of as much as 17.5 MPa can be generated at 3 km depth by this process, perhaps assisting dynamic slip weakening during the Wenchuan Earthquake.

References

Ballentine, C., and R. K. O'Nions (1994), The use of natural He, Ne, and Ar isotopes to study hydrocarbon-related fluid provenance, migration and mass balance in sedimentary basins, in *Geofluids: Origin, Migration, and Evolution of Fluids in Sedimentary Basins*, edited by J. Parnell, Geological Society Special Publication, vol. 78, pp. 347–361.

Billi, A. (2005), Gain size distribution and thickness of breccias and gouge zones form thin (<1 m) strike-slip fault cores in limestone, *J. Struc. Geol.*, 27, 1823–1837.

Boullier, A. M., K. Fujimoto, T. Ohtani, G. Roman-Ross, E. Lewin, H. Ito, P. Pezard, and B. Ildefonse (2004), Textural evidence for recent co-seismic circulation of fluids in Nojima fault zone, *Awaji Island, Japan, Tectonophysics*, 378, 165–181.

Brace, W. F., and J. D. Byerlee (1966), Stick-slip as a mechanism for earthquakes, *Science*, 153, 990–992.

Brantut, N., A. Schubnel, J.-N. Rouzaud, F. Brunet, and T. Shimamoto (2008), High-velocity frictional properties of a clay-bearing fault gouge and implications for earthquake mechanics, *J. Geophys. Res.*, 113, B10401, doi:10.1029/2007JB005551.

Brantut, N., A. Schubnel, J. Corvisier, and J. Sarout (2010), Thermochemical pressurization of faults during coseismic slip, *J. Geophys. Res.*, 115, B05314, doi:10.1029/2009JB006533.

Brantut, N., R. Han, T. Shimamoto, N. Findling, and A. Schubnel (2011), Fast slip with inhibited temperature rise due to mineral dehydration: Evidence from experiments on gypsum, *Geology*, 39(1), 59–62.

Brindley, G. W. (1952), Structural mineralogy of clays, *Clays Clay Miner.*, 1, 33–43.

Caine, J. S., J. P. Evans, and C. B. Forster (1996), Fault zone architecture and permeability structure, *Geology*, 24, 1025–1028.

Chen, J., X. Yang, J. Dang, C. He, Y. Zhou, and S. Ma (2011), Internal structure and permeability of Wenchuan earthquake fault, *Chinese J. of Geophys*, 54(7), 1805–1916. (In Chinese with an English abstract)

Chen, W.-M. D., H. Tanaka, H.-J. Huang, C.-B. Lu, C.-Y. Lee, and C.-Y. Wang (2007), Fluid infiltration associated with seismic faulting: Examining chemical and mineralogical compositions of fault rocks from the active Chelungpu fault, *Tectonophysics*, 443, 243–254.

Chester, F. M., J. P. Evans, and R. L. Biegel (1993), Internal Structure and Weakening Mechanisms of the San Andreas Fault, *J. Geophys. Res.*, 98(B1), 771–786, doi:10.1029/92JB01866.

de Meer, S., and C. J. Spiers (1997), Uniaxial compaction creep of wet gypsum aggregates, *J. Geophys. Res.*, 102(B1), 875–891, doi:10.1029/96JB02481.

De Paola, N., G. Chiodini, T. Hirose, C. Cardellini, S. Caliro, and T. Shimamoto (2011), The geochemical signature caused by earthquake propagation in carbonate-hosted faults, *Earth and Planet. Sci. Lett.*, 310, 225–232.

Famin, V., S. Nakashima, A.-M. Boullier, K. Fujimoto, and T. Hirono (2008), Earthquakes produce carbon dioxide in crustal faults, *Earth and Planet. Sci. Lett.*, 265(3-4), 487–497.

Faulkner, D. R., A. C. Lewis and E. H. Rutter (2003), On the internal structure and mechanics of large strike-slip fault zones: field observations of the Carboneras fault in southeastern Spain, Tectonophysics, 367, 235–251.

Ferri, F., G. Di Toro, T. Hirose, and T. Shimamoto (2010), Evidence of thermal pressurization in high-velocity friction experiments on smectite-rich gouges, *Terra Nova*, 00(0), 1–7.

Fondriest, M., S. A. F. Smith, G. Di Toro, D. Zampieri, and S. Mittempergher (2012), Fault zone structure and seismic slip localization in dolostones, an example from the Southern Alps, Italy, *J. Struc. Geol.*, 45, 52–67.

Fu, B., P. Wang, P. Kong, G. Zheng, G. Wang, and P. Shi (2008), Preliminary study of coseismic fault gouge occurred in the slip zone of the Wenchuan Ms 8.0 earthquake and its tectonic implications, *Acta Petrologica Sinica*, 24(10), 2237–2243. (In Chinese with an English abstract)

Goddard, J. V., and J. P. Evans (1995), Chemical changes and fluid-rock interaction in faults of crystalline thrust sheets, northwestern Wyoming, U.S.A., *J. Struct. Geol.*, 17, 533–547.

Gratier, J.-P., J. Richard, F. Renard, S. Mittempergher, M.-L. Doan, G. Di Toro, J. Hadizadeh, and A.-M. Boullier (2011), Aseismic sliding of active faults by pressure solution creep: Evidence from the San Andreas-Fault Observatory at Depth, *Geology*, 39, 1131–1134.

Grant, J. A. (1986), The isocon diagram-a simple solution to Gresens' equation for metasomatic alteration, *Econ. Geol.*, 81, 1976–1982.

Hamada, Y., T. Hirono, W. Tanikawa, W. Soh, and S.-R. Song (2009), Energy taken up by co-seismic chemical reactions during a large earthquake: An example from the 1999 Taiwan Chi-Chi earthquake, *Geophys. Res. Lett.*, 36, L06301, doi:10.1029/2008GL036772.

Han, L., Y. Zhou, J. Chen, S. Ma, X. Yang, C. He, and J. Dang (2010), Structural characters of co-seismic fault gouge in bed rocks during the Wenchuan Earthquake, *Quaternary Science*, 30(4), 746–758. (In Chinese with an English abstract)

Han, R., T. Shimamoto, and T. Hirose (2007), Ultralow friction of carbonate faults caused by thermal decomposition, *Science*, 316, 878–881.

Hausegger, S., W. Kurz, R. Rabitsch, E. Kiechl, and F.-J. Brosch (2010), Analysis of the internal structure of a carbonate damaged zone: Implications for the mechanisms of fault breccia formation and fluid flow, *J. Struc. Geol.*, 32(9), 1349–1362.

Hawkins, R. K., and P. A. Egelstaff (1980), Interfacial water structure in montmorillonite from neutron diffraction experiments, *Clays and Clay Minerals*, 28, 19–28.

Hellings, L., F. Dehairs, M. Tackx, E. Keppens, and W. Baeyens (1999), Origin and fate of organic carbon in the freshwater part of the Scheldt Estuary as traced by stable carbon isotope composition, *Biogeochemistry*, 47(2), 167–186.

Hickman, S., R. Sibson, and R. Bruhn (1995), Introduction to special section: Mechanical involvement of fluids in faulting, *J. Geophys. Res.*, 100(B7), 12,831–12,840, doi:10.1029/95JB01121.

Hirono, T., et al. (2006), Evidence of frictional melting from disk-shaped black material, discovered within the Taiwan Chelungpu fault system, *Geophys. Res. Lett.*, 33, L19311, doi:10.1029/2006GL027329.

Hirono, T., et al. (2007), A chemical kinetic approach to estimate dynamic shear stress during the 1999 Taiwan Chi-Chi earthquake, *Geophys. Res. Lett.*, 34, L19308, doi:10.1029/2007GL030743. (Correction, *Geophys. Res. Lett.*, 35, doi:10.1029/2007GL032512, 2008.)

Hirono, T., et al. (2008), Clay mineral reactions caused by frictional heating during an earthquake: An example from the Taiwan Chelungpu fault, *Geophys. Res. Lett.*, 35, L16303, doi:10.1029/2008GL034476.

Hirose, T., and M. Bystricky (2007), Extreme dynamic weakening of faults during dehydration by coseismic shear heating, *Geophys. Res. Lett.*, 34, L14311, doi:10.1029/2007GL030049

Huang, W. L., J. M. Longo, and D. R. Pevear (1993), An experimentally derived kinetic model for smectite-to-illite conversion and its use as a geothermometer, *Clays and Clay Minerals*, 41, 162–177.

Huang, W. L., W. A. Bassett, and T. C. Wu (1994), Dehydration and hydration of montmorillonite at elevated temperatures and pressures monitored using synchrotron radiation, *Am. Mineral.*, 79, 683–691.

Isaacs, A. J., J. P. Evans, S.-R. Song, and P. T. Kolesar (2007), Structural, Mineralogical, and Geochemical Characterization of the Chelungpu Thrust Fault. Taiwan, *Terr. Atmos. Ocean. Sci.*, 18(2), 183–221.

Ishikawa, T., et al. (2008), Coseimic fluid-rock interations at high temperatures in the Chelungpu fault, *Nature Geosciences*, 1, 679–683.

Jacobsen, S. D., J. R. Smyth, R. J. Swope, and R. T. Downs (1998), Rigid-body character of the SO4 groups in celestine, anglesite, and barite, *Can. Mineral.*, 36, 1053–1060.

Janssen, C., R. L. Romer, A. Hoffmann-Rothe, B. Mingram, P. Dulski, P. Moller, and H. Al-Zubi (2005), The role of fluid in faulting deformation: a case study from the Dead Sea Transform (Jordan), *Int. J. Earth Sci.*, 94, 243–255.

Johnson, K. M., A. E. King, and J. M. Sieburth (1985), Coulometric TCO$_2$ analyses for marine studies; an introduction, *Marine Chemistry*, 16(1), 61–82.

Kerr, P. F. (1952), Formation and occurrence of clay minerals, *Clays Clay Miner.*, 1, 19–32.

Kerrich, R., T. E. La Tour, and L. Willmore (1984), Fluid Participation in Deep Fault Zones: Evidence From Geological, Geochemical, and $^{18}O/^{16}O$ Relations, *J. Geophys. Res.*, 89(B6), 4331–4343, doi:10.1029/JB089iB06p04331.

Kirschner, D. L., and L. A. Kennedy (2001), Limited syntectonic fluid flow in carbonate-hosted thrust faults of the Front Ranges, Canadian Rockies, inferred from stable isotope data and structures, *J. Geophys. Res.*, 106(B5), 8827–8840, doi:10.1029/2000JB900414.

Kuo, L.-W., S.-R. Song, E.-C. Yeh, and H.-F. Chen (2009), Clay mineral anomalies in the fault zone of the Chelungpu Fault, Taiwan, and their implications, *Geophys. Res. Lett.*, 36, L18306, doi:10.1029/2009GL039269.

Labaume, P., E. Carrio-Schaffhauser, J.-F. Gamond, and F. Renard (2004), Deformation mechanisms and fluid-driven mass transfers in the recent fault zones of the Corinth Rift (Greece), *C. R. Geoscience*, 336, 375–383.

Li, C.-Y., Z.-Y. Wei, J.-Q. Ye, Y.-B. Han, and W.-J. Zheng (2010), Amounts and styles of coseismic deformation along the northern segment of surface rupture, of the 2008 Wenchuan Mw 7.9 earthquake, *China, Tectonophysics*, 491(1-4), 35–58.

Li, Y., et al. (2006), Elimination efficiency of different reagents for the memory effect of mercury using ICP-MS, *J. Anal. At. Spectrom.*, 21, 94–96.

Lin, X., F. Ying, and N. Zheng (1992), Techniques of X-ray Diffraction Analysis and Its Geological Application, pp. 119–131, Beijing: Petroleum Industry Press. (In Chinese with an English abstract)

Liu, C.-W., and W.-S. Lin (2005), A smectite dehydration model in a shallow sedimentary basin: model development, *Clays Clay Miner.*, 53(1), 55–70.

Luo, L., L. Tang, Z. Xu, and H. Li (2010), Monitor and characteristics of fluid during Chinese Wenchuan Fault Scientific Drilling, American Geophysical Union, Fall annual meeting, San Francisco, Abstract T53E-05.

Lockner, D. A., C. Morrow, D. Moore, and S. Hickman (2011), Low strength of deep San Andreas Fault gouge from SAFOD core, *Nature*, 472, 82–85.

Mishima, T., T. Hirono, W. Soh, and S.-R. Song (2006), Thermal history estimation of the Taiwan Chelungpu fault using rock-magnetic methods, *Geophys. Res. Lett.*, 33, L23311, doi:10.1029/2006GL028088.

Molli, G., et al. (2010), Fault zone structure and fluid-rock interaction of a high angle normal fault in Carrara marble (NW Tuscany, Italy), *J. Struc. Geol.*, 32, 1334–1348.

O'Hara, K. (1988), Fluid flow and volume loss during mylonitization: an origin for phyllonite in an overthrust setting, North Carolina U.S.A., *Tectonophysics*, 156(1-2), 21–36.

O'Neil, J. R., R. N. Clayton, and T. K. Mayeda (1969). Oxygen isotope fractionation in divalent metal carbonates, *J. Chem. Physics*, 51, 5547–5558.

Ohomoto, H., and R. O. Rye (1979), Isotopes of sulfur and Carbon, in *Geochemistry of Hydrothermal Ore Deposits*, edited by H. L. Barnes, pp. 509–567, New York: Wiley.

Pili, E., F. Poitrasson, and J. P. Gratier (2002), Carbon-oxygen isotope and trace element constraints on how fluids percolate faulted limestones from the San Andreas Fault system: partitioning of fluid sources and pathways, *Chem. Geol.*, 190, 231–250.

Pili, E., B. M. Kennedy, M. E. Conrad, and J.-P. Gratier (2011), Isotopic evidence for the infiltration of mantle and metamorphic CO$_2$-H$_2$O fluids from below in faulted rocks from the San Andreas Fault System, *Chem. Geol.*, 281(3-4), 242–252.

Rao, T. G., and P. K. Govil (1995), Merits of using Barium as a heavy absorber in major element analysis of rock samples by XRD: New data on ASK-1 and ASK-2 reference samples, *Analyst*, 120, 1279–1282.

Roland, P., and K. Ola (1996), Physico/chemical stability of smectite clays, *Eng. Geol.*, 41, 73–85.

Saffer, D. M., and C. Marone (2003), Comparison of smectite- and illite-rich gouge frictional properties: Application to the updip limit of the seismogenic zone along subduction megathrusts, *Earth Planet. Sci. Lett.*, 215, 219–235.

Sheppard, S. M., and H. P. Schwarcz (1970), Fractionation of carbon and oxygen isotopes and magnesium between coexisting metamorphic calcite and dolomite, *Contrib. Mineral. Petrol.*, 26(3), 161–198.

Shieh, Y. N., and H. P. Taylor (1969), Carbon and hydrogen isotope studies at contact metamorphism in the Santa Rosa Range, Nevada and other areas, *Contrib. Mineral. Petrol.*, 20, 306–356.

Sibson, R. H. (1973), Interaction between temperature and pore-fluid pressure during earthquake faulting-A mechanism for partial or total stress relief, *Nature*, 243, 66–68.

Sibson, R. H. (1990), Conditions for fault-valve behavior, *Geol. Soc., London, Special Publications*, 54, 15–28.

Sibson, R. H., F. Robert, and K. H. Poulsen (1988), High-angle reverse faults, fluid-pressure cycling, and mesothermal gold-quartz deposits, *Geology*, 16(6), 551–555.

Solum, J. G., B. A. van der Pluijm, D. R. Peacor, and L. Warr (2003), Influence of phyllosilicate mineral assemblages, fabrics, and fluids on the behavior of the Punchbowl Fault, Southern California, *J. Geophys. Res.*, 108, doi:10.1029/2002JB001781.

Sulem, J., and V. Famin (2009), Thermal decomposition of carbonates in fault zones: Slip-weakening and temperature limiting effects, *J. Geophys. Res.*, 114, B03309, doi:10.1029/2008JB006004.

Syunnan, S. (1981), Clay mineralogy, Translated by S. Yan, W. Liu, and K. Jia, Beijing: Geological Publishing House, 230 pp.(In Chinese)

Tanaka, H., K. Fujimoto, T. Ohtani, and H. Ito (2001), Structural and chemical characterization of shear zones in the freshly activated Nojima fault, Awaji Island, southwest Japan, *J. Geophys. Res.*, 106(B5), 8789–8810, doi:10.1029/2000JB900444

Tanikawa, W., T. Mishima, T. Hirono, W. Lin, T. Shimamoto, W. Soh, and S.-R. Song (2007), High magnetic susceptibility produced in high-velocity frictional tests on core samples from the Chelungpu fault in Taiwan, *Geophys. Res. Lett.*, 34, L15304, doi:10.1029/2007GL030783.

Tenthorey, E., S. F. Cox, and H. F. Todd (2003), Evolution of strength recovery and permeability during fluid-rock reaction in experimental fault zones, *Earth Planet. Sci. Lett.*, 206, 161–172.

Vrolijk, P., and B. van der Pluijm (1999), Clay gouge, *J. Struc. Geol.*, 21, 1039–1048.

Wang, P.-L., J.-J. Wu, E.-C. Yeh, S.-R. Song, Y.-G. Chen, and L.-H. Lin (2010), Isotopic constraints of vein carbonates on fluid sources and processes associated with the ongoing brittle deformation within the accretionary wedge of Taiwan, *Terra Nova*, 22, 251–256.

Wibberley, C. A. J., and T. Shimamoto (2003), Internal structure and permeability of major strike-slip fault zones: the Median Tectonic Line in Mie Prefecture, Southwest Japan, *J. Struct. Geol.*, 25, 59–78.

Wintsch, R. P., R. Christoffersen, and A. K. Kronenberg (1995), Fluid-rock reaction weakening of fault zones, *J. Geophys. Res.*, 100(B7), 13,021–13,032, doi:10.1029/94JB02622.

Xu, X., X. Wen, G. Yu, G. Chen, Y. Klinger, J. Hubbard, and J. Shaw (2009), Coseismic reverse- and oblique-slip surface faulting generated by the 2008 Mw 7.9 Wenchuan earthquake, *China, Geology*, 37(6), 515–518.

Xu, Z., and H. Li (2010), New Results from the Wenchuan Earthquake Fault Scientific Drilling Project (WFSD), American Geophysical Union, fall annual meeting, San Francisco, Abstract T53E-01.

Yang, T., J. Chen, H. Wang, and H. Jin (2012), Rock magnetic properties of fault rocks from the rupture of the 2008 Wenchuan earthquake, China and their implications: Preliminary results from the Zhaojiagou outcrop, Beichuan County (Sichuan), *Tectonophysics*, 530, 331–341.

Yao, L., T. Shimamoto, S. Ma, J. Chen, and T. Togo (2011), Internal structures and High-velocity (HV) frictional properties of Longmenshan Fault Zone at Pingxi outcrop, Sichuan, China, AOGS annual meeting, Taibei, Abstract SE83-A028.

Yasuhara, H., C. Marone, and D. Elsworth (2005), Fault zone restrengthening and frictional healing: The role of pressure solution, *J. Geophys. Res.*, 110, B06310, doi:10.1029/2004JB003327.

Zhang, P., X. Wen, Z. Shen, and J. Chen (2010), Oblique, high-angle, listric-reverse faulting and associated development of strain: The Wenchuan earthquake of May 12, 2008, Sichuan, China, *Annu. Rev. Earth Planet. Sci.*, 38, 353–382.

Zhang, X., C. J. Spiers, and C. J. Peach (2010), Compaction creep of wet granular calcite by pressure solution at 28°C to 150°C, *J. Geophys. Res.*, 115, B09217, doi:10.1029/2008JB005853.

Zhao, G., D. R. Peacor, and S. D. McDowell (1999), "Retrograde Diagenesis" of clay minerals in the Precambrian Freda sandstone, Wisconsin, *Clays Clay Miner.*, 47(2), 119–130.

Zheng, Y. F., and J. Hoefs (1993), Carbon and oxygen isotopic covariations in hydrothermal calcites, *Miner. Deposita*, 28, 79–89.

Zhou, X., et al. (2010), Geochemistry of soil gas in the seismic fault zone produced by the Wenchuan Ms 8.0 earthquake, southwestern *China, Geochem. Trans.*, 11(5), 1–10.